Microstructured Magnetoelastic Membrane for Magnetic Bioactuators and Soft Artificial Muscles Applications

Svetlana Ponomareva, Marie Carriere, Yanxia Hou, Robert Morel, Bernard Dieny, Hélène Joisten

ADVANCED INTELLIGENT SYSTEMS
Open Access
www.advintellsyst.com

Microstructured Magnetoelastic Membrane for Magnetic Bioactuators and Soft Artificial Muscles Applications

*Svetlana Ponomareva, Marie Carriere, Yanxia Hou, Robert Morel, Bernard Dieny, and Hélène Joisten**

In the growing field of mechanobiology, artificial mechano-reactive systems play an essential role in the generation of mechanical forces and control of material deformations. Free-standing magnetic nanoparticles have been studied for the mechanical stimulation of living cells. Magnetic composite materials are also used to mimic muscles at macroscale. In this study, a new magnetically actuated membrane is focused, which can be used for various applications in soft robotics or as a bioreactor. It consists of a few microns thick polydimethylsiloxane (PDMS) membrane in which an array of magnetic microdisks is embedded. These membranes have a large tuneable flexibility, and they are transparent, biocompatible, and waterproof. They are usable in biology and optics, both potentially combined. The membrane deformations under magnetic field have been experimentally characterized and modeled. By growing pancreatic cells on such membranes, it has been demonstrated that insulin production from the cells can be enhanced thanks to the mechanical stimulation of the cells provided by the actuated membrane.

1. Introduction

Actuable polymer materials,[1,2] widely investigated over the past two decades, attract an ever-growing interest in the field of robotics and biomechanics, both at macroscopic and microscopic levels. Their ability to deform and transmit physical forces to surrounding media enables the development of bioinspired systems,[3] such as artificial muscles.[4,5] In addition to the most commonly used driving mechanisms[6–8] which include electroactive, ionic, photonic, pneumatic, and shape-memory actuation, magnetically actuated polymer composites have emerged.[9,10] Their advantages lie in the potentially long range and efficient remote actuation, high stability, and low power consumption. In particular, polydimethylsiloxane (PDMS) comprising micro-/nanomagnets,[11] for example, in the form of membrane,[12,13] has recently opened the way to artificial muscle applications at macroscale[14] and soft microrobotics.[15,16]

In addition, such actuable materials enable the development of bioreactors/bioactuators.[17] Those can be used to generate physical forces on biological cells and tissues, aimed at stimulating cellular functions.[18,19] The importance of mechanical phenomena at the cell level in biology has been underlined by crucial findings, such as the receptors for touch enlightened by the 2021 Nobel Prize in medicine.[20] Moreover, targeted mechanostimulation has been explored over the past decade for potential cancer treatments,[21,22] using in particular magnetically actuated microdisks to destroy cancer cells,[23,24] as originally published by Kim et al.[25] The properties of these magnetically actuated microdisks make them particularly interesting to complement the available micromechanical tools[26] and magnetic metamaterials.[27–29]

In a recent study, we reported the development of a prototype magnetoelastic membrane (MEM) composed of a PDMS/gold bilayer (5 μm/100 nm thick) magnetically actuated thanks to embedded magnetic microdisks of permalloy ($Ni_{20}Fe_{80}$ alloy), 1.25 μm thick, placed in a regular array. This membrane acts as a flexible diffraction grating and its deformation under magnetic field has been optically characterized and modeled.[30] However, due to the high stiffness of this membrane (resulting from the gold Young's modulus of 80 GPa) and to its fragility, applications in biophysics, fluidics, and biomimicry were limited.

S. Ponomareva, R. Morel, B. Dieny, H. Joisten
Univ. Grenoble Alpes
CEA
CNRS
IRIG-SPINTEC
38000 Grenoble, France
E-mail: helene.joisten@cea.fr

M. Carriere, Y. Hou
Univ. Grenoble Alpes
CEA
CNRS
IRIG-SYMMES
38000 Grenoble, France

H. Joisten
Univ. Grenoble Alpes
CEA
Leti
38000 Grenoble, France

The ORCID identification number(s) for the author(s) of this article can be found under https://doi.org/10.1002/aisy.202300022.

DOI: 10.1002/aisy.202300022

Herein, we present a new magnetically reactive PDMS-based membrane, which overcomes these limitations, while maintaining the possibility of optically monitoring its deformation via its diffraction patterns. Consisting of a 5 μm thick PDMS layer without gold coating and embedding an array of micron-size permalloy disks, the membrane is transparent. Its elasticity is increased by 4–5 orders of magnitude compared with the previous one coated with Au. This elasticity can be tuned by playing with the density and length of the polymer molecules, and with the structure of the cross-linked polymer networks, resulting in a wide range of possible elastic modulus of PDMS,[31] for instance, 460, 830, or 1720 kPa.[32,33] The enhanced mechanical deformability enables larger deformation at weaker fields or with thinner embedded magnetic microdisks. With its new properties of transparency, biocompatibility, and waterproofness, this MEM can be used for biomimicry. In an initial experiment, we showed that the vibration of such a membrane, triggered via a rotating magnetic field of a few tens of Hz, efficiently induced insulin secretion from live pancreatic cells grown on the membrane surface (Ponomareva et al.).[34]

We show here that such membrane can be used as a soft "artificial muscle", where the membrane changes between its "contracted" or "resting" state, and an "extended" configuration characterized by a larger surface and thus a slightly reduced thickness. The deformations of these membranes are reversible and repeatable provided the system remains in the elastic regime,[35] as required for an artificial muscle.[36] We focus in particular on the deformability of the membrane and on the magnetic forces and pressure potentially transferred to environment.

In the first part, we present the mechanical and magnetic properties of the membrane separately, elasticity and driving magnetic forces being independently tunable. We report then on the characterization of the magnetic actuation of the membrane by optical means. The experimental results are fitted with by a combination of an analytical magnetomechanical model and an optical one. The models enable to predict the performance of similar magnetic actuators with different elasticity and dimension parameters, for potential applications in biomimicry and bioactuation.

2. Results and Discussion

2.1. Magnetically Actuable MEM

The MEM consists of a 5 μm thick PDMS film with centimeter-scale diameter, tunable composition (blend of two PDMS types leading to various flexibilities, as studied by Palchesko et al.),[31] embedding a regular array of permalloy microdisks, 60 nm in thickness, 1.3 μm in diameter, and a pitch of 3 μm (**Figure 1**). The plan of the disks is parallel to the membrane surface. The flexibility of the membrane, described by the modulus of elasticity (i.e., Young's modulus E), depends here essentially on the composition of the PDMS, given the absence of additional continuous metallic layer. The edge-to-edge spacing between the embedded microdisks is considered as sufficiently large to neglect their contribution to the film elasticity.[30] The membrane composition and elastic properties are presented and discussed later in Section 2.1 and 2.2. Details on the fabrication process and mechanical models are given in Section 4.1–4.3.

In a spatially nonuniform magnetic field, the embedded magnetic disks are subjected to magnetic forces generated by the field and its gradient. They are thus attracted toward areas of higher magnetic field. Hence, if the MEM is maintained by its edges on a hollow ring support and suspended in the air or in a liquid, it deforms from a planar state in zero field to a concave shape when the external nonhomogeneous magnetic field is applied. The magnetic field sources in our experimental setup are commercial neodymium–iron–boron (NdFeB) magnets.[37] These permanent magnets are parallelepipeds of dimensions $2a \times 2b \times h$ (along the X-, Y-, and Z-axes), with a magnetization $\boldsymbol{M}_{MAG}$ parallel to the Z-axis. The magnetizations will be expressed here either by $\boldsymbol{M}$ in units of $\mathrm{A\,m^{-1}}$ or by $\mu_0\boldsymbol{M}$ in teslas (T), where μ_0 is the vacuum permeability given by $\mu_0 = 4\pi \times 10^{-7}\,\mathrm{T\,m\,A^{-1}}$. The Z components of the emitted magnetic field and the field gradient (B_Z and $\mathrm{d}B_Z/\mathrm{d}Z$) generate attractive magnetic forces (F_Z) on the microdisks. In this configuration, the membrane is deformed mainly along the Z direction, toward the magnet, as sketched in Figure 1a (not to scale). Figure 1b1 shows the NdFeB magnet of macroscopic dimensions, magnetized in-plane (IP), parallel to a long edge. The magnetic field B_Z, generated on the particles, depends in particular on the magnet dimensions, shape, and orientation. For biological applications, the membrane can also constitute the bottom of a container filled with a fluid.[34] In this case, the deformation of the membrane results both from the magnetic field and from the fluid weight (hydrostatic pressure). The array of permalloy microdisks was prepared by deep ultraviolet (DUV) photolithography. The magnetic material was deposited by evaporation. This technique does not allow to deposit magnetic layers as thick as by electrodeposition but was appropriate for the range of thickness that we used (60–80 nm) and avoids the additional metal layer required for electrodeposition which would decrease the membrane flexibility. We show here that despite the small thickness (nanoscale range) of our evaporated magnetic disks, the resulting magnetic forces can activate very effectively the membrane, thanks to its high flexibility.

The main steps of the fabrication process are summarized in Figure 1d, with details given later and in Section 4.1 (PDMS) and 4.4 (magnetic particles). The top–down fabrication process based on the double resist (ma-N 2400 negative tone photoresist series (MAN)/poly(methyl methacrylate (PMMA)) previously developed in our cancer cells destruction studies,[23] leads to an array of permalloy microdisks patterned on the sacrificial PMMA resist layer. In the previous studies, magnetic disks, at this point, were released into fluidic solutions by dissolving the PMMA sacrificial layer.[23] In contrast, here the magnetic particles are kept in array on the PMMA resist, coated with PDMS. Thus, the PDMS layer, deposited on the PMMA resist by a spin-coating method, incorporates the magnetic disks array (Figure 1d5). After dissolution of the PMMA layer in acetone, a well-controlled uniform PDMS film of nominal thickness of 5 μm, with embedded magnetic disks at its bottom plane is obtained (Figure 1d6). At the end of the process, membranes with centimeter-range diameters are floating in acetone and can be collected and transferred to various types of hollow supports.

One may note at this point that the silicon wafers, used here as usual clean room substrates, could advantageously be replaced by

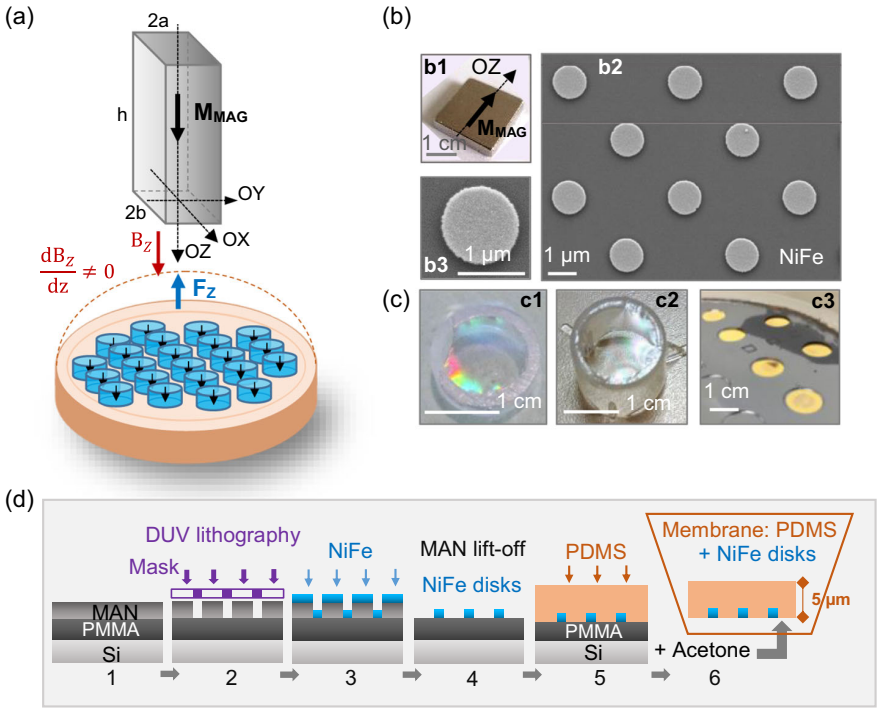

Figure 1. MEM: microstructure, actuation principle, and fabrication method. a) Sketch of the PDMS membrane with the embedded array of NiFe microdisks, bonded on a hollow support, magnetically actuated by an NdFeB magnet. b) Images of the magnetic components: b1) NdFeB magnet[37] of dimension (5 mm × 20 mm) × 20 mm, magnetization $\mu_0 M_{MAG} = 1.29$ T, used as magnetic field source. b2) Scanning electron microscopy (SEM) images of NiFe microdisks array (top view), 1.3 µm in diameter, 60 nm thick, pitch 3 µm, on Si substrate + PMMA sacrificial layer, prepared to be embedded in the PDMS layer. b3) Zoom on a particle (SEM image of a NiFe microdisk). c) Images of PDMS membranes bonded on their hollow supports: c1) PDMS membrane—5 µm thick, 1.4 cm in diameter—with embedded NiFe microdisks array, bonded on PMMA hollow tube. c2) Similar PDMS membrane without embedded magnetic particles. c3) For comparison: Au (100 nm thick)/PDMS (5 µm thick, 0.8 cm in diameter) membrane with embedded magnetic particles array, in Si hollow wafer, reproduced from publication Nanoscale,[30] with the permission of The Royal Society of Chemistry, copyright 2019. d) MEM fabrication process using microlithography and sacrificial layer, with the schematic steps: 1) spin coating of PMMA and MAN resists on Si substrate. 2) DUV lithography. 3) $Ni_{80}Fe_{20}$ deposition through evaporation. 4) Resist MAN lift-off yielding NiFe microdisks array on PMMA. 5) Spin coating of PDMS on the magnetic disks array. 6) Dissolution of the PMMA sacrificial layer: releasing the MEM from its Si substrate, which is then bonded on a hollow support.

glass wafers, given the environmental impact related to the production of silicon and its transformation into wafers.[38]

Our MEMs were bonded at the end of PMMA hollow tubes, using PDMS as glue, held by the circular edge over a hole of 14 mm diameter, as shown in Figure 1c1. In this image, the small bonding defect on the left reveals the PDMS film boundary, highlighting its transparency and reflectivity. Three types of membranes have been fabricated (Figure 1c): PDMS membranes with and without magnetic particles and the previously studied gold-colored PDMS/Au bilayer. The two first ones are optically transparent and quasi-indistinguishable by the naked eyes (Figure 1c1 and c2), whereas the third one is opaque (Figure 1c3).[30] Despite the new PDMS-based MEMs are highly transparent to the visible light, they remain reflective and diffractive, as shown further in the section related to optical characterization.

Once released from the substrate at the end of the process and attached to the hollow support, the PDMS-composite membrane embedding the magnetic disks array becomes remotely actuable. The quantification of the deformability, the involved forces, and the optical response through diffraction patterns, are presented in the next sections. We focus on the membrane actuation in a quasi-static regime, without testing its dynamic response versus frequency.

2.2. Mechanical Properties, Limit of Elasticity Regime

An advantage of PDMS is to offer a large range of elastic moduli depending on its composition, and therefore a wide range of robustness and flexibility of the membrane. The mechanical responses of the membranes were first studied on PDMS films without embedded magnetic microdisks, that is, on passive membranes. The disks array contribution to the membrane elasticity is considered negligible, as mentioned previously.

Our PDMS-based membranes were strong and waterproof enough to form the bottom of containers holding aqueous solutions such as water or cell culture medium.[34] As non-treated PDMS exhibits hydrophobic properties, a surface treatment by O_2 plasma was applied to render its surface hydrophilic.[39] The PDMS membranes mechanical properties were characterized under hydrostatic pressure, as shown in **Figure 2**. Using

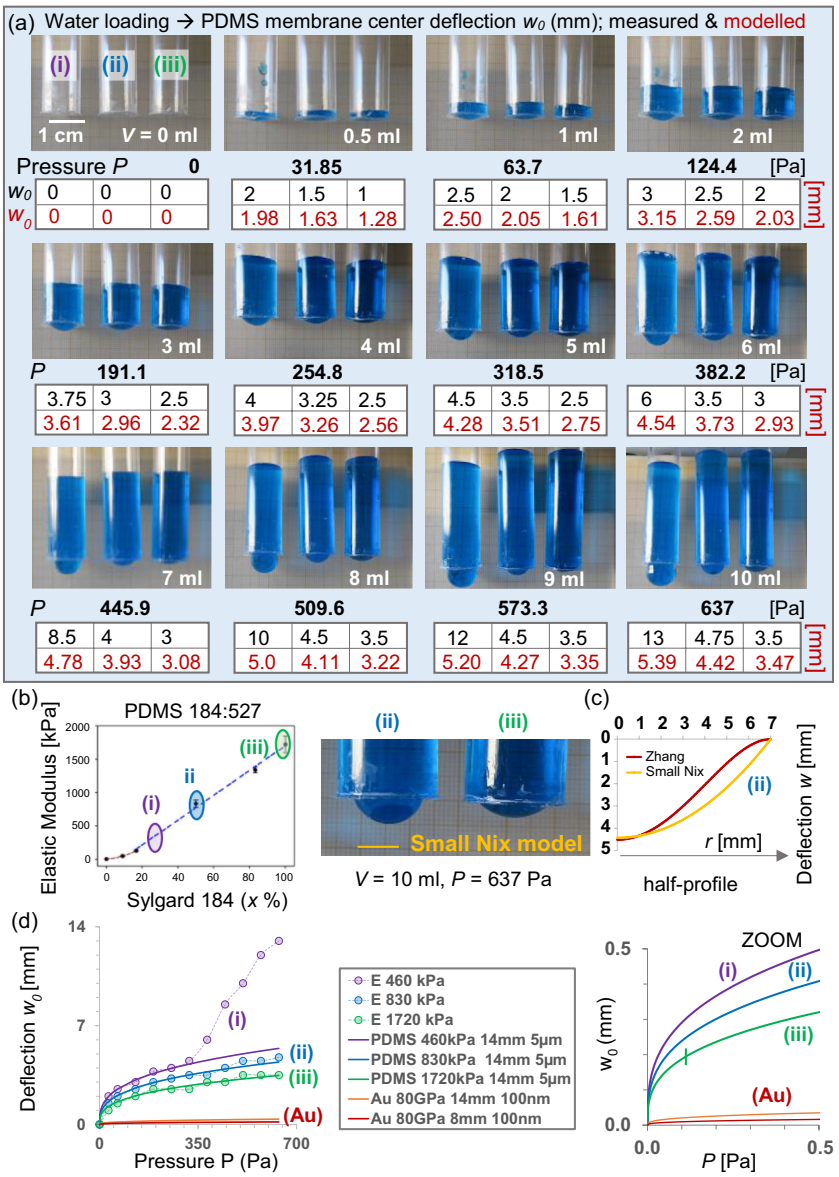

Figure 2. Mechanical characterization of 5 µm thick PDMS membranes, 14 mm in diameter, via hydrostatic pressure. Test of three PDMS compositions (i), (ii), and (iii) obtained by mixing S184 and S527. Mass ratios: (i) S184:S527 (1:2), (ii) S184:S527 (1:1), and (iii) S184 only, without embedded magnetic particles. a) Pictures of the membrane deformations, bonded to the bottom section of hollow PMMA pipes, loaded with blue-stained water of volume V from 0 to 10 mL. Membrane deflections at center w_0 [mm]: experimental (black color), calculated based on "Small-Nix" model (red color),[35] versus V (ml) and water pressure P (Pa) ($P = \rho \cdot V \cdot g/\pi R_m^2$, where $g = 9.81$ m s^{-2}, volume density $\rho = 1000$ kg m^{-3}, and membrane radius R_m). b) Elastic modulus E (= Young's modulus) of S184-S527 PDMS mixtures versus S184-percentage x (%), reproduced from Palchesko et al.,[31] with permission of PLoS One, copyright 2012, completed with color marks indicating our three compositions (i), (ii), and (iii), showing E (kPa): (i) 460, (ii) 830, and (iii) 1720 kPa, respectively. c) The membranes (ii) and (iii), loaded with $V = 10$ mL ($P = 630$ Pa); left: "Small-Nix" model half profiles, fitted to photographs; right: (ii) comparison of half-profile curves from "Small-Nix" (non-zero slope at the edge) and "Zhang" (clamped condition of zero slope) models, from Zhang.[35] d) Curves of experimental ("E"): dashed lines with circles and modeled (solid lines) deflections w_0 versus loading pressure P (Pa) for the three PDMS membranes (i), (ii), (iii), and Au/PDMS membranes previously studied.[30] The curve's colors refer to the membrane's composition, Young's modulus E, diameter, thickness, and model used, as follows: i) violet: PDMS, 460 kPa, Ø14 mm, 5 µm, Small-Nix. ii) Blue: PDMS, 830 kPa, Ø14 mm, 5 µm, Small-Nix. iii) Green: PDMS, 1720 kPa, Ø14 mm, 5 µm, Small-Nix. (Au) red: Au/PDMS, 80 GPa, Ø8 mm, 100 nm (Au thickness), Zhang. (Au) orange: Au/PDMS, 80 GPa, Ø14 mm, 100 nm (Au thickness), Zhang. Zoom: a mark on (iii) curve at ($P = 0.136$ Pa; $w_0 = 210$ µm): deflection calculated below versus magnetic forces, fitted by optical response. e) Stress–strain curves: pressure (Pa) versus strain ε (%) $= 100 \times (L - 2R_m)/2R_m$. Left: strain in logarithmic scale. Right: zoom with strain in linear scale for PDMS membranes only.

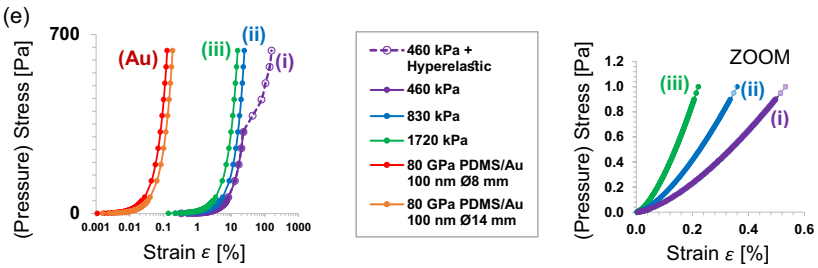

Figure 2. Continued.

an approach similar to that reported by D. Kim et al.,[40] water was dropped on PDMS membranes. The resulting membrane deformation was then quantified.

In our experimental device, membranes of fixed thickness (5 μm) and three different PDMS compositions were glued to the bottom section of PMMA pipes (see Figure 2). To characterize their deformability, the pipes were loaded with controlled volumes of blue-stained water exerting a loading pressure on the membrane and inducing a membrane deformation, as shown in Figure 2a. The membranes were composed, as proposed by Palchesko et al.,[31] of blends of two commercial PDMS: the elastomer Sylgard 184 (S184) (the stiffest), and the gel Sylgard 527 (S527) (the most flexible and soft), in various proportions. Such PDMS mixtures exhibit Young's moduli ranging from a few kPa to about 2 MPa, depending on the mass ratio of the two components, as shown in Figure 2b (reproduced from Palchesko et al.[31] and annotated). After testing PDMS of different elasticity by mixing S184 and S527, we focused on three compositions corresponding to S184 percentages x of: i) 33%, ii) 50%, and iii) 100% having expected Young's moduli E of i) 460 kPa, ii) 830 kPa, and iii) 1720 kPa, respectively, as shown in Figure 2b. These E values were corroborated by the simulation of the membrane profiles described later. For comparison, these membranes present a range of elasticity similar to those of some living tissues, such as muscle, skin, bladder, and cornea, as presented in the review by Guimarães et al.[41] This makes these membranes suitable for interacting with cells or tissues, for mimicking certain active biological behavior or for bioelectronics functions.[42]

For each water volume, the relative deformations of the three membranes (i), (ii), and (iii) can be observed in Figure 2a,c, in agreement with their relative flexibilities. The membrane made of the highest content of S527 exhibits the largest deformations. In contrast, the membrane made of 100% S184 is the least flexible and therefore the less deformed. Experimentally measured and analytically modeled values of the maximal deflections w_0 (mm) (i.e., transverse displacement of the membrane center) are plotted versus water-loading pressure P (Pa), corresponding to water volume from 0.5 to 10 mL in Figure 2d. We added the deflections curves of the significantly stiffer PDMS/Au bilayers, 8 mm diameter,[30] and 14 mm diameter for comparison with the experimental PDMS membranes (i), (ii), and (iii). Zoomed curves also focus on pressures and deformations range achieved through the magnetic actuation, detailed in the next section. The quite good agreement of the modeled deflections w_0 with the experimental measurements confirms the Young's moduli values of the PDMS blends used in the various membranes and the choice of the analytical models, described here later.

Two different analytical expressions modeling the deflection of a clamped circular plate have been used here. They both use a simplified form of the nonlinear von Karman equations of high-order derivatives, as developed by Zhang.[35] Considering the two classical bending and stretching behaviors of a membrane submitted to a loading pressure (see Boudaoud et al.),[43] a transition occurs from a bending-dominant to a stretching-dominant mode in particular when the load increases.[35] This results from the intrinsic modifications of the polymer fibers structure, displacement, or elongation, in response to the applied forces and the increasing deformations.[44] Although both modes coexist in a coupled way such as in vesicle membrane[45] or in MEM with incorporated magnetic nanoparticles,[46] various approximate expressions aim at describing the predominant mode based on the main governing (bending or stretching) energy.[35] Our assumptions and choice of models were based here on the experimentally observed membrane shape, physically related to the amplitude of the loading pressure.

The first expression, named "Small-Nix's" model,[47] describing a "stretching-dominant" behavior of the membrane,[35] has been used for modeling the hydrostatic pressure experiment. The second expression, called here the "Zhang's" model, was used for modeling the "bending-dominant" behavior of the membrane submitted to lower loading pressure such as magnetic forces in this study, and potentially the zone of "bending-stretching" transition.[35] As our PDMS-based membranes were carefully deposited on their experimental support without stretching nor compression, they were modeled without any initial IP tension.

In both models, the membrane profiles (2D cross sections) were described by the out-of-plane (OOP) displacement $w(r)$, as a function of the radial distance r from the membrane center and the maximum deflection w_0, as follows:[35]

$$w(r) = w_0 \times \left(1 - \frac{r^2}{R_m^2}\right)^i \tag{1}$$

with R_m being the membrane radius ($0 \leq r \leq R_m$) and the Small-Nix's and Zhang's equations expressing w_0 being given in Section 4.2. Two boundary conditions can describe the deformed membrane:[35] 1) The "clamped condition of zero slope," for which the membrane remains tangent to its initial plane at its circular edge, which is the case of our MEMs magnetically actuated, modeled by Zhang's expression with $i = 2$ in Equation (1) (bending behavior). 2) The "non-zero slope as clamped

condition" with $i = 1$, imposed by Small-Nix's model (spherical shape, stretching behavior), in which the membrane exhibits a positive slope at its circular edge, as observed in our water-weight experiments shown in Figure 2a,c.

As highlighted in Figure 2c, the Small-Nix's model perfectly matches the experimental profile of the PDMS membranes submitted to the hydrostatic pressure, in contrast to the "Zhang's model" with the zero-slope condition. However, both models yield quasi-identical deflections w_0 at the membrane center. The maximal deflections w_0, calculated from the Small-Nix's solution for the hydrostatic pressure on the circular membranes (i), (ii), and (iii), and from the Zhang's solution for the PDMS/Au membranes,[35] are in good agreement with the experimental measurements, as plotted in Figure 2d versus the transverse-loading pressure P_Z, for various membrane characteristics. However, the experimental deflections of the most flexible PDMS membrane (i) exhibit a sharp rise for pressures above 300 kPa, as shown by the violet dashed curve in Figure 2d. This regime of large deflection is typical of hyperelasticity.[48,49] A limit was reached, with a breaking point for a volume of water $V = 10$ mL ($P = 637$ Pa), Figure 2a showing the deformation about 1 min before the rupture of the (i) membrane. In contrast, smaller volumes of water (less than 10 mL) led to hyperelastic stretching without rupture. In this case, the membrane (i) returned to its original shape once unloaded (as visually observed). However, we did not study the potential hysteresis with loading–unloading curves,[50] as this hyperelastic regime was out of the magnetic actuation regime that we used.

In both cases, as modeled by Small-Nix's or Zhang's expressions[35] and observed experimentally, the membranes exhibited an elastic behavior as they returned to their initial planar shape at zero magnetic field or by suppressing the hydrostatic pressure.

Classically, the elastic stress in the polymer membrane balances the static-loading pressure at equilibrium. The strain ε was defined by $\varepsilon = (L\text{-}2R_m)/2R_m$, as presented by D. Kim et al.,[40] for circular PDMS membranes of microscale thicknesses. The strain's expression versus the deflection w_0 can be seen in Section 4.3, for membranes of circular arc shapes ($i = 1$ in Equation (1)). As another representation of the membranes deformability, stress–strain curves are plotted in Figure 2e. Herein, the pressure $P = P[\varepsilon(w_0)]$ was calculated i) from the Small-Nix's model in the elastic regime, ii) from experimental results of the hyperelastic behavior for the most flexible PDMS composition, and iii) for the Au/PDMS membranes approximated here only as circular arc. The logarithmic scale enables the comparison with the stiffest Au/PDMS membranes. The zoomed curves again focus on the range of magnitude used in the magnetic actuation experiments with our setup. The obtained stress–strain curves reproduce the first stages of J-shaped curves, previously observed in some earlier studies.[44,51]

To summarize this part, these preliminary hydrostatic pressure tests validated the control of the membranes elasticity and deformations, with a choice of Young's moduli based on the mixture of the two PDMS S184 and S527 achieving a trade-off between flexibility and robustness.

In the following part, we consider and evaluate the magnetic actuation of the PDMS-based MEMs. As the applied magnetic forces are lower than those exerted in the hydrostatic pressure experiments, the membrane deforms in an elastic regime without reaching hyperelasticity. We mention that in the following magnetic experiments, the particles always remained well blocked within the PDMS, the radius of curvature of the membrane being always orders of magnitude larger than the diameter of the microdisks.

2.3. Magnetic Actuation

Magnetic fields with nonzero field gradient produced by a permanent magnet were used to induce forces on the magnetic microdisks embedded in the membrane. Let us note that magnetic torques,[52,53] although more effective to actuate dispersed particles than field gradients, could not significantly contribute to the membrane deformation given the clamped edge, which prevents the membrane global rotation. Due to the relative dimensions of magnet and membrane, both centered on the Z-axis, field and field gradient and thus magnetic forces are mainly parallel to the Z-axis, when the magnet is sufficiently close. The membrane deforms essentially OOP. Residual magnetic forces in the X- or Y-directions, negligible in first approximation, are ineffective IP on a clamped membrane exhibiting small deflections. Moreover, they compensate each other in average due to the symmetry of the device around the Z-axis.[30] Therefore, we expressed the magnetic field, the magnetization of particles, and magnetic forces through their z-components only, respectively, B_Z, $\mu_0 M_Z$, and F_Z, as shown in **Figure 3**. As defined previously for the hydrostatic pressure experiments, the membrane profile can thus be characterized by the deflection $w(r)$ along the Z-axis, in response to the loading pressure resulting from the OOP magnetic forces F_Z.

In our experimental work, the MEMs were subjected to external magnetic fields generated by NdFeB permanent magnets of two different strengths $\mu_0 M_{MAG} = 1.29$ or 1.36 T, respectively, in the optical setup and in the bioreactor used to stimulate pancreatic cells described later and in more details in another study.[34] Their magnetization $\boldsymbol{M_{MAG}}$, considered uniform, is parallel to the Z-axis. The magnets are parallelepipeds of dimensions $(2a \times 2b) \times h$ parallel to the X-, Y-, and Z-axes (5 mm × 20 mm) × 20 mm in both experimental cases. They generate close to the poles, a field up to $+/-\mu_0 M_{MAG}/2$ at most. The magnetic field $B_Z(X, Y, Z)$ was measured and analytically modeled using the magnetostatic charges approach (uniform magnetic charge densities $\pm M_{MAG}$ on magnet faces perpendicular to the Z-axis). This allowed the determination of field and field gradient $\frac{\partial B_Z}{\partial Z}(X, Y, Z)$ required in the magnetic force calculation, as detailed in Section 4.5 and 4.6.

As shown in Figure 3a, experimental and modeled field and field gradient from the NdFeB magnet along the Z-axis are in good agreement. A potential way to enhance the field gradient and thus the magnetic forces exerted on microdisks at short range is shown in Figure 3a. It consists of using smaller magnets for instance of dimensions scaled down by a factor of 10, that is, (0.5 mm × 2 mm) × 2 mm, taken as an example in the force calculations later. Motorized magnets, such as spinning plates comprising embedded magnets—as previously developed and shown in the biological Section 2.5—,[34] rotating Halbach cylinders,[21] or macro- and micro-electromagnets with soft magnetic cores,[54] could then constitute sources of variable magnetic fields. They

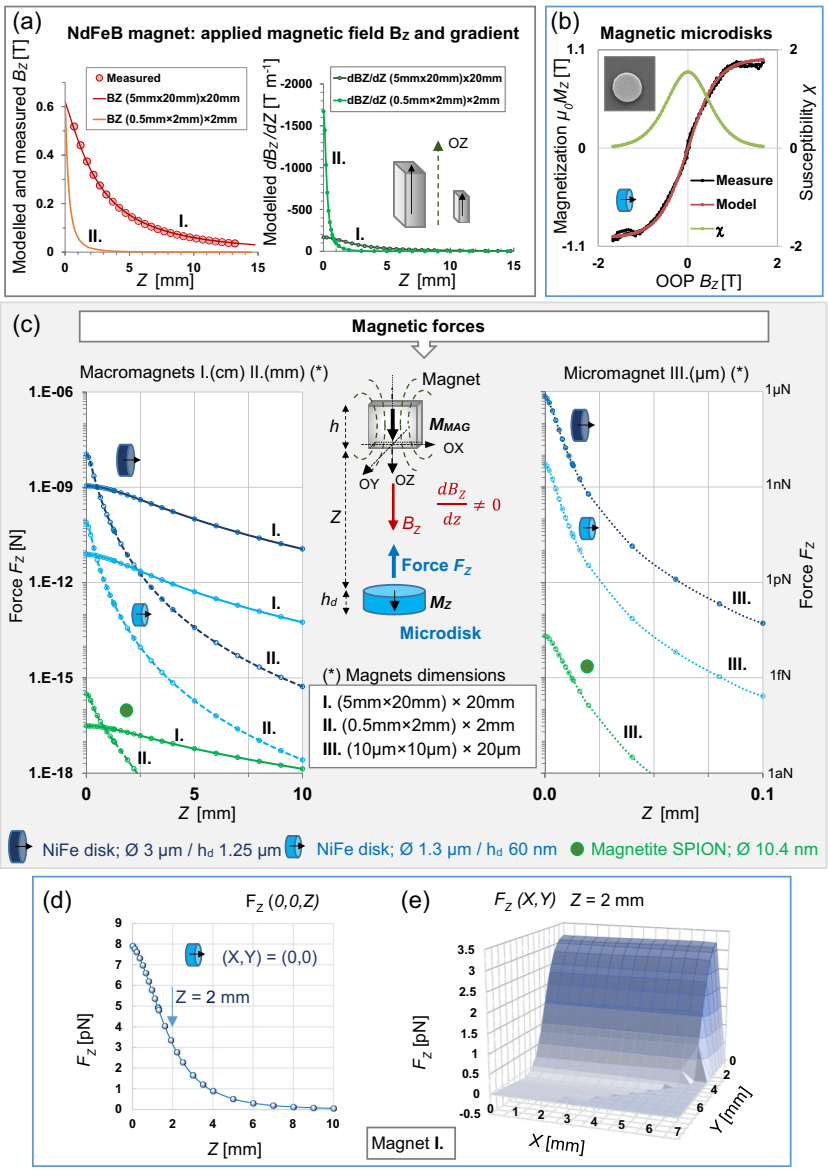

Figure 3. Magnetic forces exerted by parallelepiped magnets on magnetic micro- and nanoparticles. Analytic calculations comparing NdFeB magnets of three sizes: I (5 mm × 20 mm) × 20 mm, II (0.5 mm × 2 mm) × 2 mm, III (10 μm × 10 μm) × 20 μm, of magnetization $\boldsymbol{M_{MAG}}$ parallel to the *Z*-axis, $\mu_0 M_{MAG} = 1.29$ T, on three types of magnetic particles. a) Magnetic field B_Z and gradient dB_Z/dZ versus *Z* (distance to magnet face) along the *Z*-axis, generated by the NdFeB magnets I and II; measured and modeled for the magnet I, adapted from publication Nanoscale,[30] with the permission of The Royal Society of Chemistry, copyright 2019; model added for the magnet II. With magnet I: $B_Z = 352$ mT and $dB_Z/dZ = -108$ T m^{-1} at $Z = 1.9$ mm on the *Z*-axis. With magnet II, near the pole at $Z = 190$ μm, a similar field $B_Z = 349$ mT, and a larger gradient dB_Z/dZ of -1072 T m^{-1}; $B_Z = 19$ mT and $dB_Z/dZ = -21$ T m^{-1} only, at a similar distance $Z = 1.9$ mm. b) Experimental and modeled hysteresis loop of NiFe microdisks of diameter Ø 1.3 μm, thickness h_d 60 nm, and $Ms = 800$ kA m^{-1}: OOP magnetization $\mu_0 M_Z$ versus applied magnetic field B_Z and modeled OOP differential susceptibility $\chi = d(\mu_0 M_Z)/dB_Z$. c) Calculated magnetic forces F_Z (semi-log) exerted on a single magnetic particle on the *Z*-axis versus *Z* = distance of the point-like particle to the magnet face; magnetic field B_Z generated by the NdFeB macromagnets I and II of centimillimetric dimensions and the NdFeB micromagnet III of micrometric dimensions; B_Z calculated at the center of the particles $(Z + h_d/2)$, for three particles sizes and two compositions. Light blue curves: NiFe microdisk, $Ms = 800$ kA m^{-1}, Ø 1.3 μm, and h_d 60 nm; dark blue curves: larger NiFe microdisk, $Ms = 800$ kA m^{-1}, Ø 3 μm, and h_d 1.25 μm;[30] and green curves: magnetite SPION, Ø 10.4 nm, $Ms = 318$ kA m^{-1}, similar to SPIONs from Cursaru et al.[61]. d) Force F_Z (linear scale) by magnet I on a NiFe disk (Ø 1.3 μm, h_d 60 nm) along the Z-axis; arrow showing the magnet-to-membrane distance $Z \approx 2$ mm, that is, adjusted distance $Z \approx 1.9$ mm ($Z = 1.88$ mm), yielding $F_Z = 3.40$ pN at $(X, Y) = (0,0)$, and an average force of 1.22 pN on the membrane surface, as used in optics below. e) Mapping of the magnetic forces $F_Z(X,Y,Z)$ versus (X,Y) on ¼ membrane, with magnet I placed at $Z = 2$ mm. From (a–e), the NdFeB magnet I of 1.29 T, with $(2a \times 2b) \times h = (20 \text{ mm} \times 5 \text{ mm}) \times 20$ mm, located at $Z \approx 1.9$ mm ($Z = 1.88$ mm) from the membrane plane, generates $B_Z(0,0,Z) = 352$ mT and $dB_Z/dZ = -108$ T m^{-1}; inducing the magnetization $\mu_0 M_Z = 0.497$ T in a (Ø1.3 μm, 60 nm thick) NiFe disk, with $\chi = 1.17$; yielding the force $F_Z(0,0,Z) = 3.40$ pN; and from forces mapping, an average force $F_{Zav} = 1.22$ pN on the membrane (diameter 14 mm; embedded disks array, with a 2D pitch of 3 μm).

can generate fields of frequency sufficiently low (a few tens of Hz) for the membrane to dynamically deformed according to the field variations.

The permalloy microdisks embedded in the present PDMS-based membrane are similar to those used in some of our earlier studies.[23,25,55] Due to their circular shape, size, and aspect ratio, these disks exhibit an IP magnetic vortex configuration (Guslienko et al.).[56] At zero field, this configuration corresponds to a curling of the IP magnetization around a small central core which has an OOP magnetization. The OOP applied magnetic field B_Z induces a tilting of the IP magnetization toward the Z-direction and an enlargement of the OOP core. The experimental measurement of the average OOP magnetization M_Z as a function of the applied field intensity B_Z, by vibrating sample magnetometer (VSM), is shown in Figure 3b. A large magnetic field B_Z of around 1 T would be required to reach the OOP magnetic saturation of these vortex disks, their aspect ratio (thickness/radius) conferring a strong IP shape anisotropy. As reported previously,[30] a phenomenological model with "tanh" function (see Section 4.4) can fit the experimental hysteresis loop, whereas its derivative fits the OOP differential magnetic susceptibility, as shown in Figure 3b.

The magnetic microdisks (of small volume V_d) are considered as quasi-point particles in regard to the macroscale dimensions of the NdFeB magnet. They are characterized by their location (X, Y, Z) in the membrane and their average magnetization $\boldsymbol{M}(X, Y, Z)$—or magnetic moment $\boldsymbol{m} = V_d \cdot \boldsymbol{M}$—which depends on the local magnetic field $\boldsymbol{B}(X,Y,Z)$ produced by the NdFeB magnet, as presented previously and shown in Figure 3b. The magnetic force $\boldsymbol{F}$ exerted on a small particle of moment $\boldsymbol{m}$ in an external field $\boldsymbol{B}$ is classically derived from the magnetic potential energy $U_m = -\boldsymbol{m} \cdot \boldsymbol{B}$ of the particle. The differential form is expressed as: $-\mathrm{d}U_m = \boldsymbol{m} \cdot \mathrm{d}\boldsymbol{B} + \boldsymbol{B} \cdot \mathrm{d}\boldsymbol{m}$, the field $\boldsymbol{B}$ and thus the moment $\boldsymbol{m} = \boldsymbol{m}(\boldsymbol{B})$ being spatially variable. However, only the first term $\boldsymbol{m} \cdot \mathrm{d}\boldsymbol{B}$ represents the work of the magnetic force $\boldsymbol{F}$, transmitting a global mechanical force on the disk. For a small displacement $d\boldsymbol{r}$ of the disk, $\boldsymbol{F} \cdot d\boldsymbol{r} = \boldsymbol{m} \cdot \mathrm{d}\boldsymbol{B}$. The magnetic torque is here neglected, as discussed previously. In contrast, the second term $\boldsymbol{B} \cdot \mathrm{d}\boldsymbol{m}$ is the energy variation representing the work of internal forces on the spins (local magnetizations within the particle)—for instance rotating in the microdisk toward the Z-axis—without any global mechanical effect on the particle, as detailed by Brown (Ch.4, §2).[57] Thus, based on the NdFeB magnet and permalloy particles description, the magnetic force F_Z exerted on a disk has been expressed, as previously by, for example, Fletcher et al.,[58] Schaller et al.,[59] and Yuan et al.,[60] as follows

$$F_Z(X, Y, Z) = V_d \cdot M_Z(X, Y, Z) \cdot \frac{dB_Z(X, Y, Z)}{dz} \quad (2)$$

The expressions of the field and field gradient are shown in Section 4.5 and the force is shown in Section 4.6.

The analytical simulation of magnetic forces was carried out for three types of magnetic particles, combined to three dimensions of NdFeB magnets, as shown in Figure 3c. We theoretically evaluated the order of magnitude of forces exerted on three types of particles: 1) the thin NiFe microdisks (1.3 μm in diameter, thickness $h_\mathrm{d} = 60$ nm), embedded in the present membrane; 2) the larger NiFe disks;[30] and 3) classical spherical magnetite superparamagnetic iron oxide nanoparticles (SPIONs).[61] Three assumptions were also made on the NdFeB magnet used for the actuation: I) a macroscale magnet from the experimental setup, II) a 1/10 scaled-down magnet, and III) a microscale magnet, for comparison.

The wide range of magnetic forces and their decay rates, calculated on a single particle versus particle-to-magnet distance, is shown in Figure 3c. For instance, on the (60 nm thick, Ø1.3 μm) microdisk, at a short distance $Z = 5$ μm, the OOP force F_Z varies from 7.9 pN (magnet I), 78 pN (magnet II), to 0.86 nN (micromagnet III). Despite the relatively strong magnetic field and field gradient, combined with significant particle magnetization, the magnetic forces on each particle are still weak (e.g., pN) due to their small volume V_d (e.g., 1.3 μm diameter, thickness h_d of 60 nm: $V_\mathrm{d} \approx 8 \times 10^{-20}$ m^3). For instance, in the optical experiments, the use of the experimental macromagnet I (5 mm × 20 mm) × 20 mm at a distance $Z \approx 1.9$ mm, results in an applied magnetic field $B_Z = 352$ mT and a field gradient $|\mathrm{d}B_Z/\mathrm{d}Z| = 108$ T m^{-1}, leading to the OOP magnetization $\mu_0.M_Z = 0.497$ T in a NiFe microdisk (Figure 3b). The corresponding magnetic force on the microdisk is $F_Z = (8 \times 10^{-20}) \cdot (0.497) \cdot \mu_0^{-1} \cdot (108) \approx 3.4$ pN. The sum of the forces on all the embedded particles induces the deformation of the membrane (1.7×10^7 particles overall).

We chose the relatively stiff PDMS composition of modulus $E = 1720$ kPa (S184) in our experimental setup, with 60 nm thick microdisks and macroscale NdFeB magnet separated by a reasonable macroscale distance ($Z \approx 2$ mm), for testing and modeling the 14 mm diameter membrane actuation and optical responses. Magnetic forces involved in this optical experiment (on a single particle) have been plotted, in a linear scale, along the Z-axis (Figure 3d), and mapped on a quarter membrane at the distance $Z \approx 2$ mm (Figure 3e). Considering the whole membrane with embedded magnetic microdisks as a 2D array, the force varies from one magnetic particle to another, according to the expression $F_Z(X, Y, Z)$ of the analytical model (Equation (2)), which allows its mapping over the membrane surface. However, the "clamped circular plate" analytical models described previously (Zhang),[35] assume a uniform transverse pressure. Therefore, in the following, we made the assumption that the magnetic force distributed on the membrane is uniform, given by the average of the mapped forces. This assumption, valid in particular when the magnet covers the whole membrane surface—which is not the case here, as shown in Figure 3e, remains acceptable if the membrane is rigid enough to mechanically average its deformation, as in our PDMS S184 membrane. In other cases, numerical simulations would be required.

The resulting effective uniform pressure exerted by the magnet on the membrane was then expressed as $P_\mathrm{Z} = F_\mathrm{Zav}/(\mathrm{pitch} \times \mathrm{pitch})$, considering the pitch of the square array of embedded microdisks. Owing to the relative dimensions of the membrane and magnet and due to the relatively small magnetic forces, the membrane remains flat near its circular edge, in contrast to the shape given by the hydrostatic pressure experiment previously described. The clamped plate Zhang's model, with the zero-slope condition ($i = 2$ in Equation (1) and Section 4.2), is thus appropriate to simulate the membrane profile and to calculate its deflexion w_0 versus the magnetic pressure P_Z.

In our experimental and modeled example, the NdFeB magnet placed at $Z = 1.9$ mm from the membrane plane, generated a force $F_Z = 3.4$ pN on the Z-axis at $(X,Y) = (0,0)$. The averaged force F_{Zav}, resulted in $F_{Zav} = 1.22$ pN, as outlined at the end of Figure 3 legend. This led to the calculated pressure $P_Z = F_{Zav}/(\text{pitch} \times \text{pitch}) = 0.136$ Pa. From Zhang's model, applied on the membrane of Young's modulus $E = 1720$ kPa, Poisson's ratio $\nu = 0.49$, 5 µm thick, this magnetic transverse-loading pressure P_Z induces a deflexion $w_0 = 210$ µm at the membrane center.

At this stage, the Young's modulus E was estimated from the PDMS composition (Figure 2b)—corroborated by the good agreement between the hydrostatic pressure experiment and the membrane deformation model. We calculated the pressure P_Z exerted by the magnetic force on this membrane from the magnetic data and the magnet-to-membrane distance. The resulting 210 µm deflection of the membrane was calculated by applying the mechanical model, for this modulus E and pressure P_Z, without direct experimental measurement. We will show that this calculated deflection is experimentally validated by the optical experiment presented hereafter.

Our optical experiment and model were then tested to corroborate and assess the mechanical result, as done previously.[30] This optical method was first used on the previous opaque and reflective gold/PDMS bilayer, using the laser beam in reflection only, to quantify the membrane deformation.[30] The PDMS MEM, although highly transparent, was found to be sufficiently reflective for this optical approach.

2.4. Deformation and Optical Response of the MEM

Two optical properties of the PDMS-based membrane can be put forward. First, quasi-transparent in the range of visible light, the membrane retains its high transparency despite the presence of the embedded array of magnetic particles. Second, the invisible embedded particles array constitutes an efficient optical diffraction grating in reflexion for the laser beam. We show later that

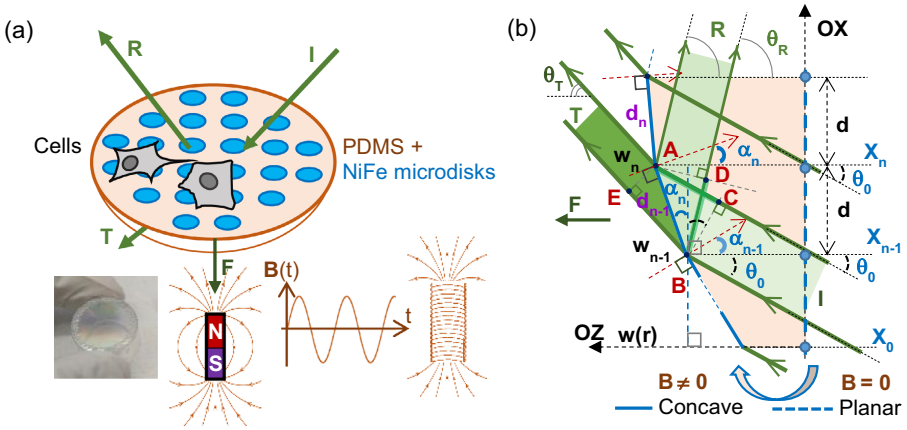

Figure 4. Optical response of the PDMS-based MEM, as a deformable diffraction grating. a) Sketch of the membrane illuminated by a laser beam (I incident, R reflected, and T transmitted), magnetically actuated and deformed by a magnet or electromagnet. The figure illustrates a potential concomitant use in biology with living cells submitted to the membrane vibrations.[34] Photo of a released MEM (Ø 14 mm) held on an annular support, ready to be used in the optical experiment. b) Scheme of the membrane and laser beam cross section, used in the optical model, reproduced and recolored from Joisten et al.,[30] with permission of Nanoscale, © The Royal Society of Chemistry 2019; θ_0 = incident angle of the laser beam on the planar membrane; directions θ of the light observation: $\theta = \theta_R$ in reflection, θ_T in transmission; d = pitch of the particles array in the planar membrane; A, B: particles of transverse deflections w_n, w_{n-1} respectively; d_{n-1} = length AB in the concave membrane; and α_n = local angle between the tilted segment AB and OX. c) Optical experiment + model. c1). Photograph of the transparent MEM maintained on a support, illuminated by a laser beam in zero magnetic field, showing the incident (I) and transmitted (T) beam spots, and the diffracted light in reflection (R) on an obliquely oriented screen. c2) Photograph of the diffraction pattern in reflexion, the illuminated membrane being deformed by the applied magnetic field B generated by the NdFeB magnet at the distance $Z = 1.9$ mm; imaged on the backside of the screen-oriented quasi-parallel to the membrane plane. c3) Light intensity profile of the diffraction pattern in reflection (imaged in c2). Experimental curve (black color): average cross section from diffraction pattern, by image analysis via ImageJ software. Modeled curve (green color): profile calculated through the analytical optical model, with a membrane deflection $w_0 = 210$ µm as input parameter, resulting from magnetic forces and elastic plate deformation calculated previously. Experiment and models parameters: PDMS-based membrane (S184) of Young modulus $E = 1720$ kPa (III), Poisson's ratio $\nu = 0.49$, diameter of 14 mm, and thickness of 5 µm. With NiFe microdisks of Ø 1.3 µm, 60 nm thick, as square array of 2D pitch 3 µm × 3 µm. NdFeB magnet of $\mu_0 M_{MAG} = 1.29$ T, dimensions (5 mm × 20 mm) × 20 mm. Distance between the membrane initial plane and the magnet face $Z = 1.9$ mm ($B_Z \approx 0.352$ T, $dB_Z/dZ \approx -108$ T m^{-1} on the Z-axis). Microdisks magnetization M_Z from the "TANH" model with $K = 1.55$. Calculated transverse-loading pressure $P_Z = 0.136$ Pa. From "clamped plate" Zhang's model: deflection $w_0 = 210$ µm and membrane concave profile with $i = 2$. In optics: Thorlabs laser CPS532-C2, wavelength $\lambda = 532$ nm; beam diameter 3.5 mm; and effective laser beam diameter $D_{eff} = 2.746$ mm (fitted with experiment). Diffracting particle diameter: $a = 1.3$ µm. Pitch on OX (grating): $d = 3$ µm. Membrane radius $R_m = 7$ mm. N_{total}, N, and n_{min} defined in Section 4.7. $N_{total} = 2R_m/d = 4667$ particles; incidence angle: $\theta_0 = \pi/30$ rd, close to normal incidence; off-centered laser beam: the first enlightened particle $n_{min} = 1000$. Number of particles enlightened on OX (average) $N = 920$. Input in the optical model: $w_0 = 210$ µm. Distance membrane-to-screen $D = 15$ cm. The light intensity curve is calculated versus X on 5000 points, with an X increment of 0.02 mm. c4) Comparison of the diffraction patterns in transmission and reflection, modeled for the same membrane deformation; red color curves: response of the planar membrane ($w_0 = 0$ µm); green color: response of the deformed membrane; left: transmission, $w_0 = -210$ µm, $\theta_0 = \pi - \pi/30$: quasi-superposed diffraction peaks; right: reflection, $w_0 = +210$ µm, $\theta_0 = \pi/30$: shift and broadening of the interference peaks for the deformed membrane (as shown in c3).

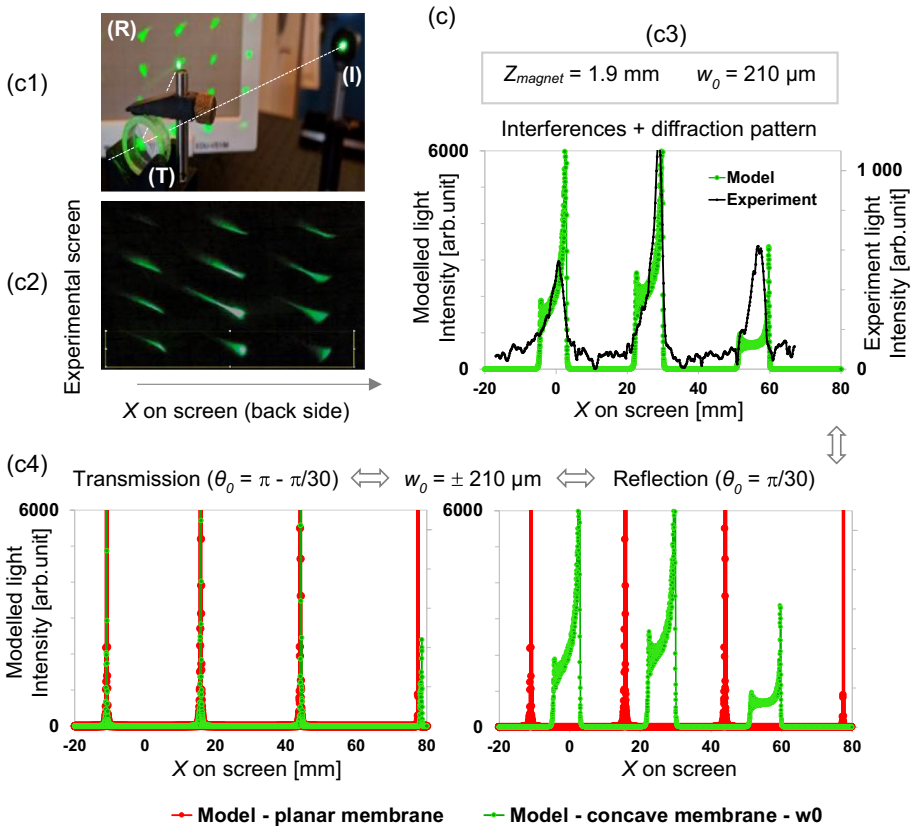

Figure 4. Continued.

these diffracting optical properties, shown in **Figure 4**, enable the characterization of the membrane deformation quantitatively interpreted by our optical interference and diffraction model.

A laser beam of wavelength $\lambda = 532$ nm, as sketched in Figure 4a, illuminates the membrane suspended on its annular support. The figure illustrates a potential use of the optical control associated with living cells stimulation, in biology.[34] As previously studied on the more rigid Au/PDMS systems,[30] the optical response of the new membrane has been studied through the diffraction patterns in reflection only, as the transmitted beam remains quasi-insensitive to the membrane deformation.

The incident laser beam is horizontal in the *XZ* plane, directed toward the membrane with an incident angle θ_0 between its direction and the *Z*-axis, as sketched in Figure 4b on the membrane profile. The membrane is modeled as a unidimensional curved optical grating lying in the *XZ* plane. As is well-known, the diffraction patterns from a planar optical grating, corresponding to the flat membrane in zero field, are similar in transmission and reflection, the brightest peak (0th order of interference) corresponding to the observation angles $\theta_T = \theta_0$ and $\theta_R = \theta_0$, respectively.

In contrast, when the membrane becomes curved, the parallelism of the transmitted rays is preserved, whereas the reflected rays are oriented in multiple directions depending on the local incidence angles influenced by the concavity of the membrane. Thus, all the transmitted rays remain parallel to each other, in the fixed direction of the laser beam (angle θ_0 with the *Z*-axis), whether the membrane is flat or deformed, whereas the reflected rays are parallel to each other only when the membrane is flat. On the curved membrane, the direction of the reflected rays differs from one particle to another, with a reflection angle equal to the effective incidence angles $\theta_0 + \alpha_n$, where α_n is the local angular tilt of the membrane from the *X*-axis (Figure 4b). Thus, the brightest peak in reflection, which was observed at $\theta_R = \theta_0$ for a planar membrane, gets shifted differently by each particle in a curved membrane, resulting in a shift and large broadening of each interference peak of the reflected diffraction pattern. In addition, the diffraction pattern then depends on the location of the illuminated area.

Our analytical optical model (Section 4.7 and Joisten et al.[30]) calculates the interference and diffraction light intensity in reflection, taking into account the shape of the magnetically deformed membrane. The differences of optical paths between the light rays reflected on adjacent disks on the deformed membrane profile (Figure 4b) are expressed in reflection (path $(BD\text{-}CA)_n$) and transmission (path $(BE\text{-}CA)_n$) for planar membrane (Equation (15) and (16)) and concave membrane (Equation (17–20)).

The experimental setup and diffraction patterns are shown in Figure 4c. The transparent membrane (in zero magnetic field) and laser source, with incident, transmitted spots, and diffraction pattern in reflection on the screen, are shown in Figure 4c1. The light beam is indicated by a white dotted line. Upon application of the field, the diffraction pattern is strongly modified, with a broadening of the diffraction peaks resulting from the

curvature of the membrane, as shown in Figure 4c2, viewed from the screen backside. Assuming the previously calculated central deflection of the membrane $w_0 \approx 210\,\mu m$, the modeled light profile in reflection exhibits a good correlation with the experimental diffraction pattern, as shown in Figure 4c3, with parameters given in the caption of Figure 4. The diffraction pattern in transmission is likewise modeled and compared with the one in reflection, for the same incident laser beam on the same deformed membrane ($w_0 = 210\,\mu m$) (see Experimental Section). When the membrane is deformed, as shown in Figure 4c4, the modeled transmission pattern remains quasi unchanged (left), whereas the interference peaks are shifted and significantly broadened in reflection (right), in agreement with the experimental observations (see Figure 4c3), and qualitatively interpreted previously. This results from the fact that in reflection (small angles approximation in Equation (17)), the optical path $(BD - CA)_n$ can be approximated by $(BD - CA)_n \sim d_{n-1} \cdot (\theta - \theta_0 - 2_{\alpha n})$ which depends on α_n, α_n representing the local tilt of the membrane. In contrast, in transmission, the optical path $(BE - CA)_n \sim d_{n-1} \cdot (\theta - \theta_0)$ is independent of α_n. Nevertheless, in transmission, a slight shift and widening of the transmission diffraction peaks is observed (see the second diffraction order peak in Figure 4c4 (left)) due to the displacement of the magnetic microparticles as the membrane deforms. This is modeled in Figure 4c4. This effect is however negligible, compared to the one produced by the variation of the incidence angles in reflection in Figure 4c4 (right).

At this stage, a combination of the magnetomechanical and optical approaches can be realized, allowing us to evaluate the magnetic actuation of the PDMS-based membrane through its optical response. The membrane was thus characterized as a two-dimensional active diffraction grating, magnetically driven.

Different experimental and theoretical configurations of membrane actuation were then compared. Various assumptions were made on the magnetoelastic properties of the membrane, magnets, and membranes dimensions. The resulting magnetic forces, loading pressures, and elastic deformations are then summarized in **Table 1**, including the data from hydrostatic pressure experiments.

2.5. Applications in Biomimicry, Artificial Muscle, and Mechanical Stimulation of Cells

Our results (Table 1) show the range of deformations that the PDMS-based MEM can reach. In particular, the experimental 14 mm diameter membrane (5 μm thick), submitted to the pressure of 0.136 Pa—from 60 nm thick microdisks array, at $Z = 1.9$ mm from the macroscale magnet I—exhibits a deflection of 210 μm at its center, corroborated by the quantitative analysis of the diffraction pattern (Figure 4). In comparison with the stiffer Au/PDMS bilayer of our previous work,[30] the deflection is increased by a factor of about 10, for a driving pressure about 10 times smaller, as a result of the reduced Young's modulus of the PDMS membrane (1720 kPa) and its larger membrane diameter.

Magnetoelastic PDMS-based membranes with embedded magnetic particles have already been described in literature. However, they are generally made of thicker polymer elements (e.g., 1 mm,[10] 167,[13] and 35 μm,[12]) and loaded with a higher density of magnetic particles. These particles are mostly made of hard magnetic materials (e.g., NdFeB or SmFeN powders),[11,13] dispersed as powder, embedded in the thick PDMS layers requiring larger forces to be actuated. We also reported on our thin (5 μm/100 nm) PDMS/Au membrane, driven by an array of thick (1.25 μm) electrodeposited magnetic particles.[30] However, this previous Au/PDMS bilayer exhibited a rather high stiffness due to the continuous gold layer which was required for the electrodeposition of the magnetic particles.[30]

Piconewton range of forces (a few pN to hundreds pN) generated by one magnetic microdisk, coincide with the range of biological muscles fiber forces, measured by Kishino and Yanagida for a single actin filament,[62] or given by Mirvakili and Hunter for myosin molecules sets.[5] Summed over the disks array with about 1.7×10^7 magnetic microdisks within our 14 mm diameter membrane, a resulting global force of tens of micronewton is exerted on the membrane surface. This is comparable with the light-induced micronewton forces from contracting gels actuating millimetric PDMS structures (Nitta et al.).[63,64] The loading pressures resulting from our magnetic actuation (0.1–6 Pa), however, turn out to be about four orders of magnitudes lower than pressures involved in natural muscle fibers at microscale, such as pressures of about 30 nN μm^{-2}, that is, 30 kPa from sarcomeres isolated from skeletal muscles.[65]

The pressure exerted from the magnetic actuation on the MEMs could be significantly increased by using magnetic sources of smaller dimensions and shorter range, such as micro- (electro-) magnets, periodically distributed in 2D arrays, as proposed by Cugat et al.,[54] and illustrated by forces from (10 μm × 10 μm) × 20 μm micromagnets in Figure 3. Thicker magnetic microdisks would likewise increase the magnetic driving force, proportionnally to the magnetic volume.

In contrast, despite the low loading pressure obtained through our macroscale magnets, the PDMS membrane has already proven effective for acting on cells and tissues. Our biological study (Ponomareva et al.),[34] on insulin secretion stimulation, is shown in **Figure 5**. In particular, as shown in Figure 5a–f, we interestingly showed that both the dispersed magnetic microdisks and the MEM can lead to an enhancement of the insulin secretion, when they are actuated by the varying magnetic field. However, due to their micro-/nanoscale dimensions, the magnetic particles, if dispersed among the pancreatic cells, can get internalized by the living cells, as illustrated by the sketch and the transmission electron microscopy (TEM) images in Figure 5a–c.[34] This invasive phenomenon, whereas appropriate for cancer cells destruction,[66] may cause adverse effects when trying to stimulate cellular functions. The advantage of the MEM used here as a bioactuator is to provide a mechanical stimulation of the cells while preventing the endocytosis of the magnetic particles, as shown in Figure 5d–f.

The deformations of the membranes shown in Table 1 are calculated from initial states which are flat, in zero transverse pressure and zero stress (in particular in zero magnetic field and without water). However, the pancreatic cells were seeded here at 1.2×10^5 cells per MEM, in 0.4 mL of culture medium.[34] This "water" volume of 0.4 mL (i.e., a pressure of 25.49 Pa) yields an initial static membrane deflection of 1842 μm (calculated by Small-Nix's model) or 1877 μm (calculated by Zhang's model). Thus, the applied magnetic field generates an additional pressure

Table 1. PDMS-based membrane deflections due to hydrostatic pressure or magnetic actuation versus loading pressures and membrane characteristics.

	Membrane stress from hydrostatic pressure			Membrane deflections w_0 [μm] [PDMS (5 μm); or Au (100 nm)][a]				
	membrane Ø [mm]	V [ml]	P_Z [Pa][b]	PDMS 460 kPa		PDMS 830 kPa	PDMS 1720 kPa	Au 80 Gpa
				Exp.[c]	Small-Nix[d]	Small-Nix[d]	Small-Nix[d]	Zhang[e]
	Ø 14	10	637 Pa	13 000[c]	5390	4420[f]	3470[f]	378
	Ø 14	9	573.3 Pa	12 000[c]	5200	4270[f]	3350[f]	365
	Ø 14	8	509.6 Pa	10 000[c]	5000	4110[f]	3220[f]	351
	Ø 14	7	445.9 Pa	8500[c]	4780	3930[f]	3080[f]	336
	Ø 14	6	382.2 Pa	6000[c]	4540	3730[f]	2930[f]	319
	Ø 14	5	318.5 Pa	4500[c]	4280[f]	3510[f]	2750[f]	300
	Ø 14	4	254.8 Pa	4000[c]	3970[f]	3260[f]	2560[f]	279
	Ø 14	3	191.1 Pa	3750[c]	3610[f]	2960[f]	2320[f]	253
	Ø 14	2	127.4 Pa	3000[c]	3150[f]	2590[f]	2030[f]	221
	Ø 14	1	63.7 Pa	2500[c]	2500[f]	2050[f]	1610[f]	176
	Ø 14	0.5	31.85 Pa	2000[c]	1980[f]	1630[f]	1280[f]	139

Magnetic actuation: magnet on 1 microdisk[g]						Magnetic actuation: on membrane[g]				Membrane deflections w_0 (μm) [PDMS (5 μm); or Au(100 nm)][a]			
magnet $\mu_0 M_{MAG}$ [T]	magnet to disk Z [μm]	disk Ø [μm]	disk thickness h_d [nm]	K (Tanh model)	F_Z (Z,0,0) on 1 disk [pN]	membrane Ø [mm]	array pitch [μm × μm]	F_{Zav} [pN]	P_Z [Pa][b]	PDMS 460 kPa	PDMS 830 kPa	PDMS 1720 kPa	Au 80 Gpa
										Zhang[e]	Zhang[e]	Zhang[e]	Zhang[e]
1.36[h]	1000[h]	Ø 1.3[h]	200[h]	K = 1.9	23.5 pN	Ø 14[h]	3 × 3[h]	9.3 pN	1.03 Pa	645[h]	529	415	44
1.36	2000	Ø 1.3	200	K = 1.9	13,6 pN	Ø 14	3 × 3	4.9 pN	0.548 Pa	521	429	336	36
1.36[h]	1000[h]	Ø 1.3[h]	60[h]	K = 1.55	6.18 pN	Ø 14[h]	3 × 3[h]	2.43 pN	0.270 Pa	412[h]	338	265	28
1.36	2000	Ø 1.3	60	K = 1.55	3.47 pN	Ø 14	3 × 3	1.25 pN	0.139 Pa	330	271	213	23
1.29	3410	Ø 3	1250	K = 2.85	240 pN	Ø 14	5 × 5	97.2 pN	3.89 Pa	1003	824	646	70
1.29	6080	Ø 3	1250	K = 2.85	58.9 pN	Ø 14	5 × 5	30.0 pN	1.20 Pa	678	557	436	47
1.29	3410	Ø 3	1250	K = 2.85	240 pN	Ø 8	5 × 5	160 pN	6.41	562	462	362	39
1.29[i]	3410[i]	Ø 3[i]	1250[i]	K = 2.85	240 pN	Ø 8[i]	hexag.[i,j]		6.0 Pa				38 [i,k]
1.29	6080	Ø 3	1250	K = 2.85	58.9 pN	Ø 8	5 × 5	45.5 pN	1.82 Pa	369	303	238	25
1.29[i]	6080[i]	Ø 3[i]	1250[i]	K = 2.85	58.9 pN	Ø 8[i]	hexag.[i,j]		1.5 Pa				23.8[i,k]
1.29[l]	1880[l]	Ø 1.3[l]	60[l]	K = 1.55	3.40 pN	Ø 14[l]	3 × 3[l]	1.22 pN	0.136 Pa	328	269	211[k,l]	23

[a]With membranes composed of either: PDMS (5 μm thick) [i] S184:S527 (1:2), $E = 460$ kPa; ii) S184:S527 (1:1), $E = 830$ kPa; iii) S184 only, $E = 1720$ kPa], or bilayer PDMS/Au: PDMS S184 (5 μm thick)/Au (100 nm thick) $E = 80$ GPa. Poisson's ratio ν: $\nu_{PDMS} = 0.49$; $\nu_{AU} = 0.42$. [b]P_Z = calculated transverse-loading pressure on membrane, either from water weight or from magnetic forces with $P_Z = F_{Zav}$/pitch × pitch [c]Deflection w_0 experimentally measured from hydrostatic pressure experiments (Figure 2), showing hyperelasticity for $P_Z > 380$ Pa. [d]Deflection w_0 calculated by Small-Nix's model. [e]Deflection w_0 calculated by Zhang's model. [f]Small-Nix's elastic model in good agreement with water-weight experiment (Figure 2). [g]Z = distance between a disk and the magnet face, along the Z-axis; F_Z (Z,0,0) = calculated magnetic force on one disk on the Z-axis; and $F_{Zav} = F_Z$ average on the disks embedded within the membrane, that is, sum of F_Z on disks/number of disks. [h]Our biological experiment (insulin release enhancement) in the study by Ponomareva et al., 2022 (comparison of two thicknesses 60 nm and 200 nm). [i]Our optical experiment (particles as hexagonal array) in the study by Joisten et al., 2019, in good agreement with magnetoelastic-optical model. [j]Exp. = experiment; hexag. = hexagonal; Ref. = reference. [k]Zhang's elastic model, with magnetic and optical models, in good agreement with optical experiment. [l]Our optical experiment (presented here, Figure 3d and 4), in good agreement with magnetoelastic-optical model.

on the membrane which is predeformed by the culture medium. The magnitudes of magnetic pressures were calculated for this biological experiment (insulin release enhancement), with the magnet-to-disk distance $Z = 1$ mm, that is, 0.270 or 1.03 Pa for magnetic forces applied on NiFe disks of thicknesses 60 or 200 nm, respectively, as given in Table 1. We have then estimated the deflection variations Δw_0 due to the sole magnetic forces, thus the amplitudes of vibrations which effectively stimulate the pancreatic cells, while taking into account the initial volume of culture medium (0.4 mL). The total pressures yield Δw_0 of only 7 μm or 25 μm, for the two NiFe disks thicknesses tested (60 or 200 nm respectively), as shown in Figure 5g,h. This vibration amplitudes of 7 or 25 μm have been sufficient to enhance the insulin release for cells grown on the MEMs.

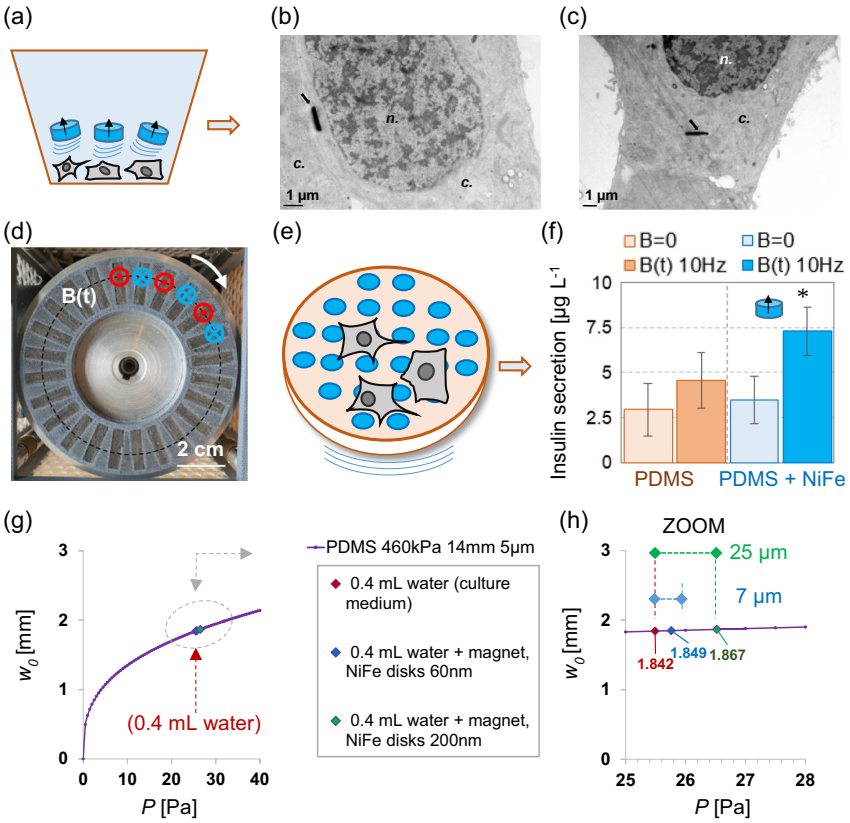

Figure 5. Application of the MEM used as soft bioactuator in mechanobiology (a to f): reproduced and adapted from Ponomareva et al.,[34] with permission from the Royal Society of Chemistry @ 2022; effects of the magnetomechanical forces generated by the permalloy microdisks (in vitro), stimulating INS-1 E pancreatic cells (a commercial cell line, originating from rat Langerhans islets and obtained from ECACC, as described in Section 4.8) (in vitro): 1) by dispersed NiFe microdisks in the fluidic culture medium (50 µg mL^{-1}) and 2) by the PDMS MEM with embedded NiFe microdisks. a) Sketch of dispersed magnetic disks vibrating on cells (not to scale). b,c) TEM images showing the cellular internalization of such NiFe disks;[34] n.: cell nucleus; c.: cell cytoplasm; arrow: NiFe disk. b) Exposed to B(t) at 20 Hz and c) exposed to B(t) at 40 Hz. d) Experimental rotating magnetic source from Platform Kinetics,[34] comprising 24 NdFeB magnets oriented up and down, $\mu_0 M_s = 1.36$ T, dimensions in Table 1. e) Sketch of the composite membrane on which the pancreatic cells are grown, actuated by the rotating field (not to scale). f) Effect of the rotating magnetic field B(t) at 10 Hz on the insulin release for cells grown on the MEMs, exposed versus control, statistical significance: $*p < 0.05$. g) Deformations of the PDMS membrane used in pancreatic cell stimulations (Young's modulus $E = 460$ kPa, 14 mm in diameter, 5 µm thick); curve of the deflection w_0 versus the transverse-loading pressure P calculated by Small-Nix's model, completed with three colored marks indicating three loading pressures: (1. red) 25.49 Pa, from 0.4 mL of culture medium (water-weight) only; (2. blue) 25.49 Pa + 0.270 Pa (from 0.4 mL of water + magnetic forces on 60 nm thick NiFe microdisks array; (3. green) 25.49 Pa + 1.03 Pa (from 0.4 mL of culture medium + magnetic forces on 200 nm thick NiFe microdisks array, experimental parameters being listed in Table 1, note 8. h) Zoomed curve exhibiting the membrane deflections of 7 and 25 µm (above the 1842 µm deflection due to the culture medium), resulting from magnetic forces on 60 and 200 nm thick disks respectively. From Small-Nix's model: 1842, 1849, and 1867 µm. From Zhang's model: 1877, 1884, and 1902 µm; Δw_0 (due to magnetic forces) of ≈7 and 25 µm for both models.

The PDMS material was also chosen for its durability.[31] Within the elastic limit (below the hyperelasticity threshold, shown in Figure 2), the membrane deformations were reproducible when adding or removing water volumes. In the biological experiment, membranes with seeded cells were placed 48 h in the incubator before the magnetic actuation, with no leakage of culture medium or visible aging.[34] Membranes of types (ii) and (iii)—shown in Figure 2a—were kept intact for 7–10 days with water volumes of 1–6 mL. The durability under hydrostatic pressure is at least a few days (2–7). Then, the periodic vibrations produced by the magnetic excitation were stable over time, yielding reproducible effects on the cells. At the frequency of 40 Hz for 30 min, the number of 72 000 cycles indicates a minimum value of the cyclic endurance (within the elastic limit shown in Figure 2d,e). However, this endurance may actually be much longer.

The membranes can be used as transparent substrates of tunable bending for cells growth, their transverse deflections being about 1–10 times larger than typical size of biological cells (20 µm). In these biological applications, the PDMS optical transparency enables the cells cultured on the membrane to be observed in transmission optical microscopy, potentially combined with an optical monitoring of the membrane deformation through the diffraction patterns in reflection. The membrane can be viewed here as a mobile substrate for cell culture, partially mimicking the mechanical behavior and continuous movements of the living environments. Cells grown on the MEM, stimulated by the membrane deformations, may thus be subjected to forces

and strains similar to those they would be exposed to in the body, in particular from muscles tissues.

These actuable membranes may also find applications in optics,[30,67,68] for instance, in the process of accommodation in the natural vision: the mechanism of cornea deformations, induced by the ciliary muscles contraction,[69] could be partially reproduced by an actuation of this transparent MEM mimicking the natural lens or cornea. A bioinspired lens of magnetically controlled focus could potentially emerge, to be compared with the "muscle-like electroactive elastomers" developed by Carpi et al.,[68] or adaptive lenses analyzed by Ren and Wu,[67] with the advantage of a remote actuation.

There is a growing interest in flexible substrates with optically controlled deformation for biological and medical sciences, as well as in astronomy (e.g., mirrors), electronics, as previously summarized.[30] Here, nanostructured magnetic disks array offers contactless actuation, whereas various other actuation principles require contact, such as pneumatic actuation for deformable PDMS-based diffraction gratings, shown in Song et al.'s review,[70] or voltage for piezoelectric actuators (Bonora et al.),[71] or mechanical traction for PDMS-based grating with nanostructured gold stripes of Hamouda et al.[72]

3. Conclusion

The objective of this study was to develop and characterize a new MEM consisting of a PDMS membrane comprising an array of magnetic nanodisks and demonstrate its potential as a magnetic actuator, both for biology and soft artificial muscles applications. We first quantified the membrane deformability under hydrostatic pressure. The large membrane deformations produced by hydrostatic pressure allowed us to quantify the membrane deformations, test its robustness, and determine the breakdown pressures. Analytical bending–stretching models were developed to interpret these experiments. The deformation under magnetic forces was then investigated. To more accurately characterize the membrane deformation, an optical approach was then used based on the observation of the diffraction patterns produced in reflection by the array of micromagnets embedded in the membrane. An optical model was developed to interpret the diffraction patterns from the curved membrane and thereby quantify the membrane deformation. Thus, our analytical models enable the quantification of static forces and pressures exerted on the membrane and its resulting deformation. These models should also be relevant in the case of low-frequency vibrations (quasi-static mode) used in mechanobiology. In particular, the forces and deformations involved in our study on the stimulation of insulin secretion, using rotating fields of 10–40 Hz (Ponomareva et al.),[34] were calculated. They are comparable to forces acting at cell level in living tissues. This membrane, remotely operated, could thus imitate a moving or vibrating cellular environment.

In summary, this magnetoelastic biocompatible and transparent membrane can be used to act on its environment in a controlled way by remotely applied magnetic field. Potential applications include bioinspired systems such as soft artificial muscles or magnetic actuator for living cells stimulation.

4. Experimental Section

4.1. Fabrication Process of the Magnetoelastic Membrane: Preparation of PDMS materials of various compositions leading to the membranes (i), (ii), and (iii). The three PDMS compositions (i), (ii), and (iii) were prepared by mixing two types of PDMS:[31,33] Sylgard 184 (S184) silicon elastomer and Sylgard 527 (S527) dielectric gel, both from Dow Corning, each of them prepared as recommended by the manufacturer.[33,73]

S184 was prepared by mixing prepolymer base and cross-linking in 10:1 mass proportion (S184).[32,73]

S527 was prepared by mixing part A and part B in 1:1 mass proportion (S527).

Each mixture was manually stirred for 5 min and then degassed for 45 min.

The mixture of the two PDMS was then spin coated on the substrate (see step 5 in Figure 1d), at the speed of 5000 rpm during 100 s, resulting in the PDMS thickness of 5 μm. The spin-coater plate was heated at 100 °C to cure the PDMS layer at the curing temperature of 100 °C during a curing time of 15 min.[73]

4.2. Mechanical Models of the Membrane Deformation:

Parameters in the Following Zhang's and Small-Nix's Models: The mechanical properties of the PDMS-based membranes, and PDMS/Au bilayer membranes, were calculated using the following parameters: the transverse-loading pressure P_Z, Young's modulus E, Poisson's ratio ν, membrane thickness h_m, membrane radius R_m, and membrane (or "plate") bending stiffness D_S

where $D_S = (E \times h_m^3)/(12 \times (1-\nu^2))$.

The water pressure (Figure 2) $P_w = (\rho_w \times [V_{ml} \times 10^{-6}] \times g)/[\pi \times R_m^2]$, used as "transverse loading pressure", is an input in the elastic plate model[35] which calculates the membrane deflections w_0, for each Young modulus E. The membrane radius $R_m = 7$ mm, water volume V_{ml} (varying from 0 to 10 mL), water density $\rho_w \approx 1000\ \mathrm{kg\ m^{-3}}$, and gravitational constant $g = 9.81\ \mathrm{m\ s^{-2}}$ are given parameters.

Our three PDMS membranes (i), (ii), and (iii) shown in Figure 2, resulted from mixtures with proportions x% of S184 and $(100-x)$% of S527, such as (i) $x = 33$%, (ii) $x = 50$%, and (iii) $x = 100$%. 1) PDMS: $E = 460$ kPa (i); or 830 kPa (ii); or 1.72 MPa (iii); $\nu = 0.49$; $h_{PDMS} = 5$ μm; and $R_m = 7$ mm. 2) Gold: $E = 80$ GPa; $\nu = 0.42$; $h_{AU} = 100$ nm; and $R_m = 4$ mm used in Joisten et al.[30] and here for comparison. In Joisten et al.,[30] the 100 nm thick gold layer governed the bilayer PDMS/Au elasticity.

Small-Nix's Model: This model simulates the hydrostatic pressure experiment on the PDMS-based membranes, as follows: the deformed membrane has a spherical shape given in Equation (1), $[w(r) = w_0 \cdot (1 - r^2/R_m^2)^i]$ with $i = 1$ and the maximal deflection w_0 being the solution of the expression[35]

$$\frac{(7-\nu)}{6} \times \frac{w_0^3}{h_m^2} = \frac{P_Z \times R_m^4}{(24 \times D_S \times (1+\nu))} \tag{3}$$

Small-Nix's model imposes one limit condition: the "non-zero slope as clamped condition", as $i = 1$ in Equation (1), appropriate for the stretching behavior of sufficiently flexible membranes, with sufficient load.

Zhang's Model: This model simulates the magnetic actuation of the PDMS-based MEMs (i), (ii), and (iii), and the previous PDMS/Au bilayers,[30] as follows: the membrane deformation is given in Equation (1), $[w(r) = w_0 \cdot (1 - r^2/R_m^2)^i]$ with $i = 2$ and the maximal deflection w_0 being the solution of the expression:[35]

$$w_0 + (0.4118 + 0.25\,\nu - 0.16088\,\nu^2) \times (w_0^3/h_m^2) = (P_Z \times R_m^4)/(64 \times D_S) \tag{4}$$

We chose $i = 2$ in Equation (1) for the magnetic actuation, as the deformations remain "small", that is, the "clamped condition of zero slope", for which the membrane remains tangent to its initial plane at its circular edge. (Zhang's model enabling two potential limit conditions, zero ($i = 2$) and non-zero ($i = 1$) slope, respectively, for the bending state and the bending–stretching transition.)[35]

4.3. Strain: In the strain expression $\varepsilon = (L - 2R_m)/2R_m$, the length L of the circular arc modeling the deformed membrane profile is expressed as a function of the membrane radius R_m and its central deflection w_0. The deflexion w_0 derives either from the Small-Nix model calculation or from the experimental data in case of hyperelasticity. The circular arc forming the membrane profile is on a circle of radius R, defined by the following geometrical relations:

$R^2 = R_m^2 + (R - w_0)^2$; with if $R_m > w_0$, $L = 2.R.\theta$, and $\mathrm{tg}\theta = Rm/(R - w_0)$, leading to the circular arc length $L = \left(\frac{R_m^2 + w_0^2}{w_0}\right) \cdot \tan^{-1}\left(\frac{2 \cdot R_m \cdot w_0}{R_m^2 - w_0^2}\right)$, leading to the strain ε expressed as

$$\begin{cases} \varepsilon = -1 + \left(\dfrac{R_m^2 + w_0^2}{2 \cdot R_m \cdot w_0}\right) \cdot \tan^{-1}\left(\dfrac{2 \cdot R_m \cdot w_0}{R_m^2 - w_0^2}\right), & \text{for} \quad R_m > w_0. \\ \varepsilon = -1 + \left(\dfrac{R_m^2 + w_0^2}{2 \cdot R_m \cdot w_0}\right) \cdot \left[\pi - \tan^{-1}\left(\dfrac{2 \cdot R_m \cdot w_0}{w_0^2 - R_m^2}\right)\right], & \text{for} \quad R_m < w_0 \\ \varepsilon = -1 + \dfrac{\pi}{2}, & \text{for} \quad R_m = w_0 \end{cases} \tag{5}$$

4.4. Magnetic Microdisks:

Patterning Process and Magnetic Material Deposition: The array of permalloy microdisks was fabricated by optical (DUV) lithography and magnetic material deposition (Figure 1d), in the 1000 class clean room PTA (Upstream Technological Platform),[74] as follows: i) a MAN resist layer (Photoresist Series ma-N 2400, using ma-N 2403 here) was spin coated onto the sacrificial PMMA layer, for the DUV lithography step; ii) a lithography process was used to open an array of cylindrical wells in the MAN resist layer (diameters of 1.3 µm); and iii) the permalloy material ($Ni_{80}Fe_{20}$) was deposited by evaporation at a rate of 0.25 nm s^{-1} (thickness of 60 nm). This process consisted of heating a material target by electron bombardment in a vacuum chamber so that the material evaporates and recondenses on the substrate. The advantage of evaporation over other deposition techniques (e.g., such as sputtering) was that the deposition was more directional, which made it easier to fill the wells of a MAN resist; iv) the lift-off of the MAN resist, using a solvent (ethanol or isopropanol) that did not dissolve the PMMA layer. At this stage, the magnetic microdisks were arranged in an array on the PMMA layer, ready to receive the PDMS layer. After the deposition of the 5 µm thick PDMS layer, the sacrificial PMMA layer was dissolved with acetone, releasing the PDMS membrane with the embedded magnetic particles from the Si substrate.

Saturation Magnetization of the NiFe Microdisks: With the particles still attached to the PMMA layer, on the Si substrate, the global magnetic properties of the magnetic microdisks arrays were measured by VSM. The resulting OOP hysteresis loops (Figure 3b), confirmed the expected value of the saturation magnetization, $M_S \approx 800$ kA m^{-1}, that is, $\mu_0 M_S \approx 1$ T, ($\mu_0 = 4\pi \times 10^{-7}$), typical of NiFe films. The OOP saturation field of the magnetic microdisks B_{ZSAT} is here ≈1 T (Figure 3b), whereas the IP saturation field of such NiFe disks would be only ≈20 mT.[55]

Model of the Magnetic NiFe Microdisks and SPIONs Magnetization: The phenomenological model with "tanh" function can fit the experimental hysteresis loop, as previously shown for NiFe particles of diameter 3 µm and thickness 1.25 µm in Joisten et al.,[30] based on the expression

$$\mu_0 M_Z = \mu_0 M_S \times \tanh(K \times B_Z)) \tag{6}$$

where $\mu_0 M_S = 1$ T and the phenomenological constant $K = 1.55$ (Figure 3b); or 1.90; or 2.85,[30] or 11, respectively, for NiFe disks of (diameter, thickness): (1.3 µm, 60 nm); (1.3 µm, 200 nm); or (3 µm, 1.25 µm); or (1 µm, 4 µm). The OOP differential magnetic susceptibility is derived from Equation (6) as follows: $d(\mu_0 M_Z)/d(B_Z) = K/\cosh^2(K \times B_Z)$ and shown in Figure 3b, used in the magnetic force model below, for $B_Z \to 0$. The SPIONs magnetization is expressed by a Langevin model as

$$\mu_0 M_Z = \mu_0 M_S \times \left(\coth(k \times B_Z) - \frac{1}{k \cdot B_Z}\right) \tag{7}$$

where $\mu_0 M_S = 0.4$ T and $k = 68$.

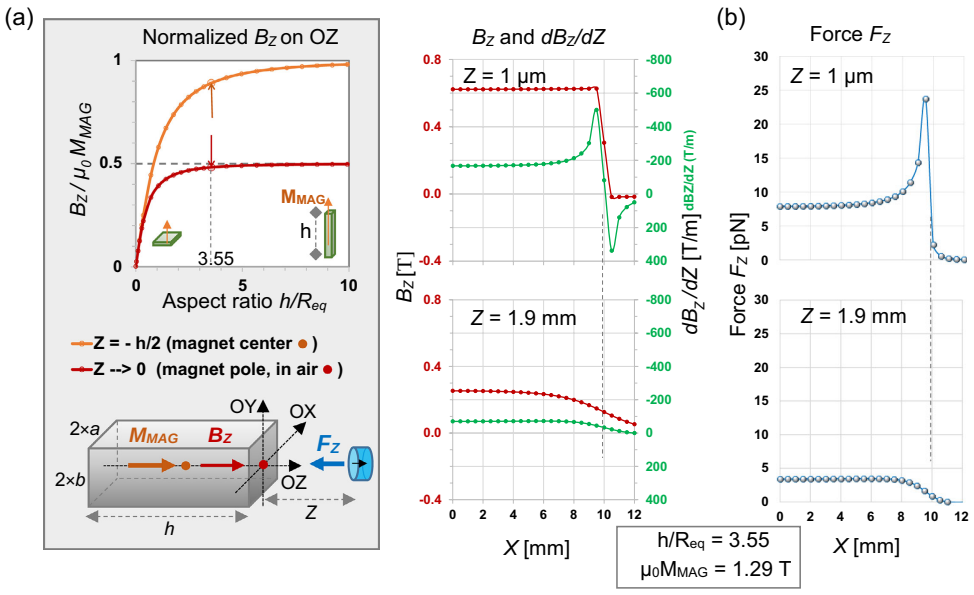

Figure 6. Magnet characteristics and typical magnetic forces. a) Magnetic field generated by a magnet as a function of its aspect ratio. Parallelepiped magnets of cross section (2a × 2b) = (20 mm × 5 mm), varying the magnet length h parallel to the Z-axis. Curves of normalized $B_Z/\mu_0 M_{MAG}$ on the Z-axis, [$X, Y = 0,0$] versus the aspect ratio h/R_{eq}, where the equivalent radius R_{eq} is defined by the section $\pi \times R_{eq}^2 = 2a \times 2b$. The two arrows indicate the experimental magnet location (ratio 3.55); i) orange curve: $B_Z/\mu_0 M_{MAG}$ calculated inside the magnet at the center ($Z = -h/2$); ii) red curve: outside near the magnet face ($Z \to 0$), showing the maximum field available on the OZ axis in air. b) Magnetic field, field gradient, and forces on a particle (Ø 1.3 µm; 60 nm thick), modeled along the transverse X-axis, for $Z = 1$ µm (close to the magnet face) and $Z = 1.9$ mm (as used in the optical experiment). With the experimental NdFeB magnet of $\mu_0 M_{MAG} = 1.29$ T, dimensions (20 mm × 5 mm) × 20 mm, aspect ratio $h/R_{eq} = 3.55$, $B_{ZMAX}(0,0,Z \to 0) \approx 0.622$ T, close to the maximum 0.5 × 1.29 T.

Permalloy microdisks and SPIONs shown in Figure 3c are characterized by: 1) the present NiFe microdisks, $\mu_0 M_S = 1$ T, diameter 1.3 μm, and thickness 60 nm; 2) larger NiFe microdisks studied in Joisten et al.,[30] $\mu_0 M_S = 1$ T, diameter 3 μm, and thickness 1.25 μm; 3) spherical magnetite SPIONs, similar to those studied in Cursaru et al.,[61] $\mu_0 M_S = 0.4$ T (average magnetization here for one particle) and diameter 10.4 nm.

4.5. Source of Magnetic Field:

NdFeB Magnets: Our permanent magnets, commercial magnets from Supermagnete,[37] were composed of NdFeB, with a protective Nickel-plated coating (Ni–Cu–Ni). These magnets were parallelepipeds of 20 mm × 20 mm × 5 mm, similar to the "Q-20-20-05-N" of the Supermagnete catalog. However, the direction of their magnetization $\boldsymbol{M_{MAG}}$ was custom made by Supermagnete, adapted to our experimental setup: $\boldsymbol{M_{MAG}}$ was oriented along one of the long sides of the magnet (20 mm), thus defining the *Z*-axis direction. Magnet characteristics are shown in **Figure 6**. The aspect-ratio dependence is shown in Figure 6a, with *h* being the height along the direction of the magnetization $\boldsymbol{M_{MAG}}$ and *Req* being the equivalent radius of the magnet cross section. Two close magnetization amplitudes (from magnets of grades N42 to N45)[37] were used: $\mu_0 M_{MAG} = 1.29$ T or 1.36 T, due to their respective origins: i) from Supermagnete for the optical experiment[37] and ii) provided by Platform Kinetics for the biological application,[75] respectively.

Model of the Generated Magnetic Field and Field Gradient: The magnetic field on the *Z*-axis B_Z and the component dB_Z/dZ of the magnetic field gradient was expressed using the classical electrostatic-like field model, previously restricted to $B_Z(X,0,Z)$ in Joisten et al.,[30] extended here to $B_Z(X,Y,Z)$. By the integration of

$$\vec{B}(X,Y,Z) = \frac{\mu_0 M_{MAG}}{4\pi}.\left[\iint \frac{(X-x)dxdy}{\left(\sqrt{(X-x)^2+(Y-y)^2+Z^2}\right)^3}.\vec{i} + \iint \frac{(Y-y)dxdy}{\left(\sqrt{(X-x)^2+(Y-y)^2+Z^2}\right)^3}.\vec{j} + \iint \frac{Z.dxdy}{\left(\sqrt{(X-x)^2+(Y-y)^2+Z^2}\right)^3}.\vec{k}\right]$$

Generated by the parallelepiped magnet of dimensions $(2a \times 2b) \times h$ and magnetization $\boldsymbol{M_{MAG}}$, B_Z is expressed as a sum of two fields of opposite directions at the point (*X*,*Y*,*Z*), as follows[30]

$$B_Z(X,Y,Z) = [b_Z(X,Y,Z) - b_Z(X,Y,(Z+h))] \tag{8}$$

where $b_Z(X,Y,Z)$ and $b_Z(X,Y,(Z+h))$ are generated, respectively, by the nearest and farest charged magnet faces, separated by the magnet length *h* along the *Z*-axis parallel to the magnetization direction. After integration, each field b_Z is expressed as the sum of four terms in $\tan^{-1}$, with the magnet dimensions and the position coordinates, such as

$$b_Z(X,Y,Z) = \left(\frac{\mu_0 M_{MAG}}{4\pi}\right) \times \left[\tan^{-1}\left(\frac{(X+a)\cdot(Y+b)}{Z\cdot\left(\sqrt{(X+a)^2+(Y+b)^2+Z^2}\right)}\right) - \tan^{-1}\left(\frac{(X-a)\cdot(Y+b)}{Z\cdot\left(\sqrt{(X-a)^2+(Y+b)^2+Z^2}\right)}\right) - \tan^{-1}\left(\frac{(X+a)\cdot(Y-b)}{Z\cdot\left(\sqrt{(X+a)^2+(Y-b)^2+Z^2}\right)}\right) + \tan^{-1}\left(\frac{(X-a)\cdot(Y-b)}{Z\cdot\left(\sqrt{(X-a)^2+(Y-b)^2+Z^2}\right)}\right)\right] \tag{9}$$

The magnetic field gradient $\frac{\partial B_Z}{\partial Z}(X,Y,Z) = \left[\frac{\partial b_Z(X,Y,Z)}{\partial Z} - \frac{\partial b_Z(X,Y,(Z+h))}{\partial Z}\right]$, is extensively written by derivation of Equation s (8,9), as follows

$$\frac{\partial B_Z}{\partial Z}(X,Y,Z) = \left[\frac{\partial b_Z(X,Y,Z)}{\partial Z} - \frac{\partial b_Z(X,Y,(Z+h))}{\partial Z}\right] \tag{10}$$

Setting the intermediate function $f_Z(x,y,Z) = \frac{\partial}{\partial Z}\left[\tan^{-1}\left(\frac{x\cdot y}{Z\cdot\left(\sqrt{x^2+y^2+Z^2}\right)}\right)\right]$ resulting in: $f_Z(x,y,Z) = \frac{(-1)\cdot x\cdot y\cdot(x^2+y^2+2\cdot Z^2)}{(x^2+Z^2)\cdot(y^2+Z^2)\cdot\left(\sqrt{x^2+y^2+Z^2}\right)}$

The component $\frac{\partial B_Z}{\partial Z}(X,Y,Z)$ can be analytically written, as follows

$$\begin{aligned}&\frac{\partial b_Z(X,Y,Z)}{\partial Z} - \frac{\partial b_Z(X,Y,(Z+h))}{\partial Z}\\ &= \left(\frac{\mu_0 M_{MAG}}{4\pi}\right) \times [[f_Z((X+a),(Y+b),Z)\\ &\quad - f((X-a),(Y+b),Z) - f((X+a),(Y-b),Z)\\ &\quad + f((X-a),(Y-b),Z)] - [f_Z((X+a),(Y+b),(Z+h))\\ &\quad - f((X-a),(Y+b),(Z+h)) - f((X+a),(Y-b),(Z+h))\\ &\quad + f((X-a),(Y-b),(Z+h))]]\end{aligned} \tag{11}$$

Likewise partially written, as follows: (12)

$$\begin{aligned}&\frac{\partial b_Z(X,Y,Z)}{\partial Z}\\ &= \left(\frac{\mu_0 M_{MAG}}{4\pi}\right) \times (-1)\\ &\quad \times \left[\frac{(X+a)\times(Y+b)\times[(X+a)^2+(Y+b)^2+2\times Z^2]}{[(X+a)^2+Z^2]\times[(Y+b)^2+Z^2]\times\sqrt{[(X+a)^2+(Y+b)^2+Z^2]}}\right.\\ &\quad - \frac{(X-a)\times(Y+b)\times[(X-a)^2+(Y+b)^2+2\times Z^2]}{[(X-a)^2+Z^2]\times[(Y+b)^2+Z^2]\times\sqrt{[(X-a)^2+(Y+b)^2+Z^2]}}\\ &\quad - \frac{(X+a)\times(Y-b)\times[(X+a)^2+(Y-b)^2+2\times Z^2]}{[(X+a)^2+Z^2]\times[(Y-b)^2+Z^2]\times\sqrt{[(X+a)^2+(Y-b)^2+Z^2]}}\\ &\quad \left. + \frac{(X-a)\times(Y-b)\times[(X-a)^2+(Y-b)^2+2\times Z^2]}{[(X-a)^2+Z^2]\times[(Y-b)^2+Z^2]\times\sqrt{[(X-a)^2+(Y-b)^2+Z^2]}}\right]\end{aligned} \tag{12}$$

The magnets used in optical (here and previously)[30] and biological[34] experiments were composed of NdFeB, of two types N40 and N42, with respective magnetization $\mu_0 M_{MAG} = 1.29$ T and 1.36 T. The latter (N42) was the one used in the instrumentation developed by Platform Kinetics Limited (Dr Thomas Oliver Myers), Leeds, UK[75] Both of dimensions $(2a \times 2b) \times h = (5\text{ mm} \times 20\text{ mm}) \times 20$ mm.

In the working space (outside the magnet, near the poles), the permanent magnet of magnetization M_{MAG} generates a magnetic field B_Z—proportional to the magnetization $\mu_0 M_{MAG}$—at most equal to $\pm(0.5 \times \mu_0 M_{MAG})$ along the *Z*-axis. The field B_Z tends to $\mu_0 M_{MAG}$ in the magnet center (not accessible). These field maxima, reached only if the magnet is sufficiently long, depend on the aspect ratio of the magnet, as shown in Figure 6a. The present experimental magnets—NdFeB with $\mu_0 M_{MAG}$ of about 1.3 T—are dimensioned with a length *h* of 20 mm and a cross-sectional area $(2a \times 2b)$ of (20 mm × 5 mm), leading to a maximum field B_Z of about 0.62 T in the working space near the poles ($Z \leq 1$ μm) (B_Z in Figure 3a and 6b). A length *h* of 50 mm would enable a maximum of ≈0.65 T. The transverse variation of the field, along the *X*-axis, reveals edge effects, close to the magnet face (see $Z = 1$ μm in Figure 6b).

4.6. Magnetic Force F_Z Exerted on a Magnetic Particle: The analytical model of the magnetic forces is given in Equation (2). In short, F_Z is expressed as $F_Z(X,Y,Z) = V_d \times M_Z \times \left(\frac{dB_Z}{dz}\right)$, where the field $B_Z = \mu_0 H_Z$ is applied by the magnet on a microdisk of magnetization $M_Z = M_Z(B_Z)$, located at the distance *Z* from the magnet face, V_d being the magnetic disk volume, and H_Z being "the magnetic field intensity" in A m^{-1}. If $B_Z \to 0$, $M_Z = \chi(0)\cdot H_Z$, with $\chi(0)$ being the initial OOP susceptibility (slope of the hysteresis loop in $B_Z = 0$), in Figure 3b. In particular, the

force F_Z can be expressed in the two boundary conditions on the applied magnetic field B_Z, as follows

$$F_Z \to V_d \cdot \chi(0) \cdot \mu_0^{-1} \cdot B_Z \cdot \frac{dB_Z}{dz}, \quad \text{for} \quad B_Z \to 0, \quad \text{and}$$
$$F_Z = V_d \cdot M_{SAT} \cdot \frac{dB_Z}{dz}, \quad \text{for} \quad B_Z \geq B_{SAT} \tag{13}$$

Here, B_{SAT} being the field above which the magnetic particle is saturated.

With: i) OOP magnetization M_Z in Equations (6) or (7); ii) OOP differential magnetic susceptibility $\chi = dM_Z/dB_Z$; iii) field B_Z expressed in Equation (8) and (9); and iv) gradient dB_Z/dZ expressed in Equation (10) and (11). Figure 6b shows the order of magnitude of the forces at two distances from the magnet ($Z = 1$ µm and $Z = 1.9$ mm), in piconewton, along the transverse X-axis, based on the field and field gradient. Edge effects are highlighted for $Z = 1$ µm, close to the magnet.

4.7. Optical Model: The MEM—as deformable diffraction grating—is locally illuminated by the laser beam, as sketched in **Figure 7**.

Our analytical optical model, previously described in Joisten et al.,[30] calculated the diffraction pattern in reflection, and its evolution when the membrane was deformed by the applied magnetic field. To complement Joisten et al.,[30] the difference between diffraction patterns in transmission and reflection had been analyzed in depth and modeled. In short, based on the scheme in Figure 4b, each microdisk (of indice n on the X-axis) presents a transverse displacement w_n (along the Z-axis), the membrane shape being modeled by Equation (1) with $i = 2$ and $r = X_n - R_m$, leading to

$$w_n = w(X_n - R_m) = w_0 \cdot [1 - ((X_n - R_m)^2 / R_m^2)]^2 \tag{14}$$

The concave membrane profile is locally defined by the tilted straight line segment AB, its angle α_n with the X-axis, and its length $AB = d_{n-1}$: $\tan \alpha_n = (w_n - w_{n-1})/d$ and $\cos \alpha_n = d/d_{n-1}$ (Figure 4b).

The light intensity distribution, in the diffraction patterns, results from the sum of the light waves at the detection points, in the observation directions θ, with $\theta = \theta_T$ in transmission or $\theta = \theta_R$ in reflection (Figure 4b). The resulting intensity is based on the phase differences of the waves transmitted or reflected by neighboring particles of the grating, that is, on the optical path differences between two adjacent light rays, $(BD–CA)_n$ in reflection and $(BE–CA)_n$ in transmission, as expressed later in Equation (15) and (16) (planar membrane) and Equation (17–20) (concave membrane).

Optical Path Differences, from Two Neighboring Particles, Reflection and Transmission (Figure 4b): θ_0 being the incident angle on the planar membrane and θ being the direction of observation, for a reflected or a transmitted beam, the optical path differences between two rays from two neighboring particles A and B (Figure 4b) of the planar or concave grating, are expressed as follows:

Planar membrane

$$\text{in reflection}: BD - CA = d \cdot (\sin\theta - \sin\theta_0) \tag{15}$$

$$\text{in transmission}: BE - CA = d \cdot (\sin\theta - \sin\theta_0) \tag{16}$$

Concave membrane, in reflection

$$(BD - CA)_n = d_{n-1} \cdot (\sin(\theta - \alpha_n) - \sin(\theta_0 + \alpha_n)), \text{ developed as} \tag{17}$$

$$(BD - CA)_n = d \cdot (\sin\theta - \sin\theta_0) - (w_n - w_{n-1}) \cdot (\cos\theta + \cos\theta_0) \tag{18}$$

Concave membrane, in transmission

$$(BE - CA)_n = d_{n-1} \cdot (\sin(\theta + \alpha_n) - \sin(\theta_0 + \alpha_n)), \text{ developed as} \tag{19}$$

$$(BE - CA)_n = d \cdot (\sin\theta - \sin\theta_0) + (w_n - w_{n-1}) \cdot (\cos\theta - \cos\theta_0) \tag{20}$$

Modeling the Transmitted Light Distribution from the Reflection Expression: Equation (18) (reflection) is transformed into Equation (20) (transmission), by replacing the incident angle θ_0 by $\pi - \theta_0$ and the maximal deflection w_0 by $-w_0$, that is, replacing $(w_n - w_{n-1})$ by $-(w_n - w_{n-1})$.

Analytical Expression of the Light Distribution in Reflection (usable for Transmission): The path difference between two adjacent light rays reflected on the particles $n-1$ and n (Figure 4b), is expressed in Equation (18), taking into account the local concavity of the membrane.

From the direction of observation θ, the light distribution $U(\theta)$ (wavenumber $k = 2\pi/\lambda$) is reflected on N particles, and summed up as:[30] $U(\theta) = U^{(0)}(\theta) \cdot \left[1 + \sum_{n=1+n_{min}}^{n_{min}+(N-1)} e^{-ik\cdot(BD-CA)_n}\right]$, resulting in

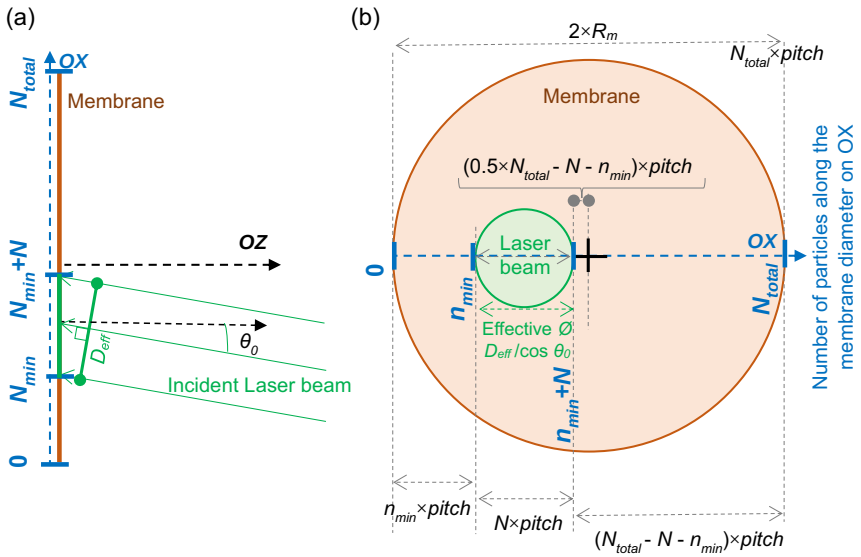

Figure 7. Sketch of the vertical MEM (flat in zero magnetic field) and horizontal incident laser beam (green color) showing particle numbers used for summing the light distribution reflected on N particles. a) Top view. b) Front view. Modeling the optical diffraction pattern from Figure 4: $R_m = 7$ mm; pitch = 3 µm; and effective diameter $D_{eff} = 2.746$ mm. $N_{total} = 2R_m/\text{pitch} = 4667$ particles; $n_{min} = 1000$ particles ($n_{min} \times$ pitch = 3 mm); $N = 920$ particles ($N \times$ pitch = 2.76 mm); and $N_{total} - N - n_{min} = 2747$ particles ($Nt_{otal} - N - n_{min}$) × pitch = 8.24 mm). (The laser enlightening $N = 920$ particles would have been centered if $n_{min} = (Nt_{otal} - N)/2 = 1873$.).

$$U(\theta) = U^{(0)}(\theta) \cdot \sum_{n=n_{\min}}^{n_{\min}+(N-1)} e^{-ik\,[n\cdot d\cdot(\sin\theta-\sin\theta_0)-w_n\cdot(\cos\theta+\cos\theta_0)]} \quad (21)$$

where, as sketched in Figure 7, the particles on the membrane diameter (on the *X*-axis), being either inside or outside the laser beam, are numbered as follows: N_{total} = total number of particles on the membrane diameter (along OX); $N_{\text{total}} = 2R_m/d$; and N = number of particles enlightened by the laser beam on the *X*-axis. To calculate N, we considered both the incident angle θ_0 and an effective laser beam diameter D_{eff} with an intensity profile supposed uniform, D_{eff} slightly smaller than the laser diameter of 3.5 mm and Gaussian intensity profile, such as: $N = (D_{\text{eff}}/\cos\theta_0) \times (1/d)$, where the pitch $d = 3$ µm. In the present experiment $\theta_0 = \pi/30\,rd$; $\cos\theta_0 \approx 0.995$ (close to normal incidence); $D_{\text{eff}} \approx 2.746$ mm; $n_{\min}$ = the first particle enlightened by the laser beam, on the membrane diameter (*X*-axis). If $n_{\min} < 0.5 \times (N_{\text{total}} - N)$, the laser beam center is on the left side of membrane center. N_{total}, $n_{\min}$, and N fitting the experimental diffraction profile are shown in the caption of Figure 7. The interference-diffraction pattern is then represented by the light intensity: $I(\theta) = [U(\theta) \cdot \overline{U(\theta)}]$, modulated by $I^{(0)}(\theta) = (U^{(0)}(\theta))^2$, that is, the Fraunhofer diffraction on the particles of diameter *a*

$I^{(0)}(\theta) = (\text{sinc}(k \cdot a \cdot p/2))^2$, with $p = \sin\theta - \sin\theta_0$,[76] and $\theta = a\tan(x/D)$, to express the light intensity versus *x* along the *X*-axis on the screen (at the membrane-to-screen distance D). This modeled light intensity is plotted in Figure 4c3,c4 (green and red color curves).

4.8. Membrane Used as Bioreactor: The study of insulin release from INS-1 E β-islet pancreatic cells, induced via the mechanical stimulation of the cells, cells being subjected to the treatments 48 h after seeding,[34] was previously described in Ponomareva et al.[34] In particular, the cell culture, the insulin secretion stimulation protocol, the cell viability and apoptosis assessment, and the characterization of the insulin secretion by cells grown on magnetoelastic membranes, compared with cells stimulated by dispersed particles, were thoroughly detailed and discussed in Ponomareva et al.[34]

The used cells were INS-1 E pancreatic cells,[34] originating from rat (*Rattus Norvegicus*) Langerhans islets. Therefore, there was no ethical issue with their use.

This commercial cell line was obtained from European Collection of Authenticated Cell Cultures (ECACC), operated by Public Health England.

Acknowledgements

The authors would like to thank the EU's H2020 Fet Open Abiomater No 665440 and H2020 ERA-Net Euronanomed II Nanoviber for their financial support.

Conflict of Interest

The authors declare no conflict of interest.

Data Availability Statement

The data that support the findings of this study are available from the corresponding author upon reasonable request.

Keywords

magnetic actuation, magnetic bioactuators, magnetic microdisks, magnetoelastic membranes, mechanobiology, microstructured composite polymers, soft artificial muscles

Received: January 12, 2023
Revised: May 24, 2023
Published online:

[1] M. A. C. Stuart, W. T. S. Huck, J. Genzer, M. Müller, C. Ober, M. Stamm, G. B. Sukhorukov, I. Szleifer, V. V. Tsukruk, M. Urban, F. Winnik, S. Zauscher, I. Luzinov, S. Minko, *Nat. Mater.* **2010**, *9*, 101.
[2] T. Manouras, M. Vamvakaki, *Polym. Chem.* **2017**, *8*, 74.
[3] S. Palagi, P. Fischer, *Nat. Rev. Mater.* **2018**, *3*, 113.
[4] B. Tondu, *Actuators* **2015**, *4*, 336.
[5] S. M. Mirvakili, I. W. Hunter, *Adv. Mater.* **2018**, *30*, 1704407.
[6] M. Shi, E. M. Yeatman, *Microsystems Nanoeng.* **2021**, *7*, 95.
[7] J. Wang, D. Gao, P. S. Lee, *Adv. Mater.* **2021**, *33*, 2003088.
[8] M. Taghavi, H. Y. Chen, A. T. Conn, J. Rossiter, *Adv. Funct. Mater.* **2022**, *32*, 2200994.
[9] J. Thévenot, H. Oliveira, O. Sandre, S. Lecommandoux, *Chem. Soc. Rev.* **2013**, *42*, 7099.
[10] M. Lee, T. Park, C. Kim, S. M. Park, *Mater. Des.* **2020**, *195*, 10.
[11] E. Fontana, L. Motyckova, C. Tomba, F. O. Keller, G. Groza, M. Bonfim, L. Ranno, T. Devillers, N. M. Dempsey, *IEEE Trans. Magn.* **2022**, *58*, 5.
[12] F. Pirmoradi, L. Cheng, M. Chiao, *J. Micromech. Microeng.* **2010**, *20*, 7.
[13] M. M. Said, J. Yunas, R. E. Pawinanto, B. Y. Majlis, B. Bais, *Sens. Actuators, A Phys.* **2016**, *245*, 85.
[14] E. Ventura, C. Oztan, D. Palacios, I. I. Vargas, E. Celik, *Funct. Mater. Lett.* **2019**, *1*, 1950089.
[15] S. Jeon, A. K. Hoshiar, K. Kim, S. Lee, E. Kim, S. Lee, J. Y. Kim, B. J. Nelson, H. J. Cha, B. J. Yi, H. Choi, *Soft Robot.* **2019**, *6*, 54.
[16] X. Wang, G. Mao, J. Ge, M. Drack, G. S. Cañón Bermúdez, D. Wirthl, R. Illing, T. Kosub, L. Bischoff, C. Wang, J. Fassbender, M. Kaltenbrunner, D. Makarov, *Commun. Mater.* **2020**, *1*, 67.
[17] Q. Shi, H. Liu, D. Tang, Y. Li, X. Li, F. Xu, *NPG Asia Mater.* **2019**, *11*, 21.
[18] Y. Sapir-Lekhovitser, M. Y. Rotenberg, J. Jopp, G. Friedman, B. Polyak, S. Cohen, *Nanoscale* **2016**, *8*, 3386.
[19] P. Campsie, P. G. Childs, S. N. Robertson, K. Cameron, J. Hough, M. Salmeron-sanchez, P. M. Tsimbouri, P. Vichare, M. J. Dalby, S. Reid, *Sci. Rep.* **2019**, *9*, 12944.
[20] S. S. Ranade, S. H. Woo, A. E. Dubin, R. A. Moshourab, C. Wetzel, M. Petrus, J. Mathur, V. Bégay, B. Coste, J. Mainquist, A. J. Wilson, A. G. Francisco, K. Reddy, Z. Qiu, J. N. Wood, G. R. Lewin, A. Patapoutian, *Nature* **2014**, *516*, 121.
[21] C. Naud, C. Thébault, M. Carrière, Y. Hou, R. Morel, F. Berger, B. Diény, H. Joisten, *Nanoscale Adv.* **2020**, *2*, 3632.
[22] L. Peixoto, R. Magalhães, D. Navas, S. Moraes, C. Redondo, R. Morales, J. P. Araújo, C. T. Sousa, *Appl. Phys. Rev.* **2020**, *7*, 30.
[23] S. Leulmi, X. Chauchet, M. Morcrette, G. Ortiz, H. Joisten, P. Sabon, T. Livache, Y. Hou, M. Carrière, S. Lequien, B. Dieny, *Nanoscale* **2015**, *7*, 15904.
[24] M. Goiriena-Goikoetxea, D. Muñoz, I. Orue, M. L. Fernández-Gubieda, J. Bokor, A. Muela, A. García-Arribas, *Appl. Phys. Rev.* **2020**, *7*, 011306.
[25] D.-H. Kim, E. A. Rozhkova, I. V. Ulasov, S. D. Bader, T. Rajh, M. S. Lesniak, V. Novosad, *Nat. Mater.* **2010**, *9*, 165.
[26] W. Xi, T. B. Saw, D. Delacour, C. T. Lim, B. Ladoux, *Nat. Rev. Mater.* **2019**, *4*, 23.
[27] D. Louis, D. Lacour, M. Hehn, V. Lomakin, T. Hauet, F. Montaigne, *Nat. Mater.* **2018**, *17*, 1076.
[28] S. Wu, W. Hu, Q. Ze, M. Sitti, R. Zhao, *Multifunct. Mater.* **2020**, *3*, 042003.
[29] A. D. M. Charles, A. N. Rider, S. A. Brown, C. H. Wang, *Prog. Mater. Sci.* **2021**, *115*, 100705.

[30] H. Joisten, A. Truong, S. Ponomareva, C. Naud, R. Morel, Y. Hou, I. Joumard, S. Auffret, P. Sabon, B. Dieny, *Nanoscale* **2019**, *11*, 10667.
[31] R. N. Palchesko, L. Zhang, Y. Sun, A. W. Feinberg, *PLoS One* **2012**, *7*, 51499.
[32] S. H. Jeong, S. Zhang, K. Hjort, J. Hilborn, Z. G. Wu, *Adv. Mater.* **2016**, *28*, 5830.
[33] M. P. Wolf, G. B. Salieb-Beugelaar, P. Hunziker, *Prog. Polym. Sci.* **2018**, *83*, 97.
[34] S. Ponomareva, H. Joisten, T. Francois, C. Naud, R. Morel, Y. Hou, T. O. Myers, I. Joumard, B. Dieny, M. Carrière, *Nanoscale* **2022**, *14*, 13274.
[35] Y. Zhang, *Sci. China Physics, Mech. Astron.* **2016**, *59*, 624602.
[36] L. Xu, Q. Peng, Y. Zhu, X. Zhao, M. Yang, S. Wang, F. Xue, Y. Yuan, Z. Lin, F. Xu, X. Sun, J. Li, W. Yin, Y. Li, X. He, *Nanoscale* **2019**, *11*, 8124.
[37] Supermagnete, https://www.supermagnete.fr/eng/block-magnets-neodymium.
[38] E. Drezet, EcoInfo CNRS GDS, **2010**.
[39] K. Efimenko, W. E. Wallace, J. Genzer, *J. Colloid Interface Sci.* **2002**, *254*, 306.
[40] Y. D. Kim, S. H. Kim, J. Y. Park, *Polymers* **2019**, *11*, 15.
[41] C. F. Guimarães, L. Gasperini, A. P. Marques, R. L. Reis, *Nat. Rev. Mater.* **2020**, *5*, 351.
[42] Y. Zhou, X. Zhao, J. Xu, Y. Fang, G. Chen, Y. Song, S. Li, J. Chen, *Nat. Mater.* **2021**, *20*, 1670.
[43] A. Boudaoud, P. Patrício, Y. Couder, M. Ben Amar, *Nature* **2000**, *407*, 718.
[44] Y. Ma, X. Feng, J. A. Rogers, Y. Huang, Y. Zhang, *Lab Chip* **2017**, *17*, 1689.
[45] R. Lipowsky, *Adv. Colloid Interface Sci.* **2014**, *208*, 14.
[46] C. A. Brisbois, M. Tasinkevych, P. Vázquez-Montejo, M. O. De La Cruz, *Proc. Natl. Acad. Sci. U. S. A.* **2019**, *116*, 2500.
[47] M. K. Small, W. D. Nix, *J. Mater. Res.* **1992**, *7*, 1553.
[48] S. K. Melly, L. Liu, Y. Liu, J. Leng, *Int. J. Mech. Syst. Dyn.* **2021**, *1*, 71.
[49] A. Srivastava, C. Y. Hui, *Proc. R. Soc. A Math. Phys. Eng. Sci.* **2013**, *469*, 13.
[50] A. P. S. Selvadurai, M. Shi, *Int. J. Non. Linear. Mech.* **2012**, *47*, 228.
[51] K. Mitsuhashi, S. Ghosh, H. Koibuchi, *Polymers* **2018**, *10*, 715.
[52] R. M. Erb, J. J. Martin, R. Soheilian, C. Pan, J. R. Barber, *Adv. Funct. Mater.* **2016**, *26*, 3859.
[53] S. Leulmi, H. Joisten, T. Dietsch, C. Iss, M. Morcrette, S. Auffret, P. Sabon, B. Dieny, *Appl. Phys. Lett.* **2013**, *103*, 132412.
[54] O. Cugat, S. Basrour, C. Divoux, P. Mounaix, G. Reyne, *Sensors Actuators, A Phys.* **2001**, *89*, 1.
[55] H. Joisten, T. Courcier, P. Balint, P. Sabon, J. Faure-Vincent, S. Auffret, B. Dieny, *Appl. Phys. Lett.* **2010**, *97*, 253112.
[56] K. Y. Guslienko, V. Novosad, Y. Otani, H. Shima, K. Fukamichi, *Appl. Phys. Lett.* **2001**, *78*, 3848.
[57] W. F. Brown, in *Magnetostatic Principles In Ferromagnetism*, North-Holland Publishing, Amsterdam **1962**, pp. 1–202.
[58] D. Fletcher, *IEEE Trans. Magn.* **1991**, *27*, 3655.
[59] V. Schaller, U. Kräling, C. Rusu, K. Petersson, J. Wipenmyr, A. Krozer, G. Wahnström, A. Sanz-Velasco, P. Enoksson, C. Johansson, *J. Appl. Phys.* **2008**, *104*, 093918.
[60] T. Yuan, Y. Yang, W. Zhan, D. Dini, *Int. J. Mol. Sci.* **2023**, *24*, 2534.
[61] L. M. Cursaru, R. M. Piticescu, D. V. Dragut, R. Morel, C. Thébault, M. Carrière, H. Joisten, B. Dieny, *Nanomaterials* **2020**, *10*, 1500.
[62] A. Kishino, T. Yanagida, *Nature* **1988**, *334*, 74.
[63] H. Hess, *Nat. Mater.* **2021**, *20*, 1040.
[64] T. Nitta, Y. Wang, Z. Du, K. Morishima, Y. Hiratsuka, *Nat. Mater.* **2021**, *20*, 1149.
[65] F. C. Minozzo, B. M. Baroni, J. A. Correa, M. A. Vaz, D. E. Rassier, *Sci. Rep.* **2013**, *3*, 2320.
[66] Y. Cheng, M. E. Muroski, D. C. M. C. Petit, R. Mansell, T. Vemulkar, R. A. Morshed, Y. Han, I. V. Balyasnikova, C. M. Horbinski, X. Huang, L. Zhang, R. P. Cowburn, M. S. Lesniak, *J. Control. Release* **2016**, *223*, 75.
[67] H. Ren, S. T. Wu, *Appl. Sci.* **2018**, *8*, 1085.
[68] F. Carpi, G. Frediani, S. Turco, D. De Rossi, *Adv. Funct. Mater.* **2011**, *21*, 4152.
[69] L. Dong, A. K. Agarwal, D. J. Beebe, H. Jiang, *Nature* **2006**, *442*, 551.
[70] W. Song, A. E. Vasdekis, D. Psaltis, *Lab Chip* **2012**, *12*, 3590.
[71] S. Bonora, F. Frassetto, E. Zanchetta, G. Della Giustina, G. Brusatin, L. Poletto, *Rev. Sci. Instrum.* **2012**, *83*, 5.
[72] F. Hamouda, A. Aassime, H. Bertin, P. Gogol, B. Bartenlian, B. Dagens, *J. Micromech. Microeng.* **2017**, *27*, 7.
[73] I. D. Johnston, D. K. McCluskey, C. K. L. Tan, M. C. Tracey, *J. Micromech. Microeng.* **2014**, *24*.
[74] PTA - Upstream Technological Platform, http://pta-grenoble.com/.
[75] Dr Thomas Oliver Myers, Platform Kinetics Limited, Leeds, UK.
[76] M. Born, E. Wolf, in *Principles of Optics*, Cambridge University Press, Cambridge UK **1959**.